Wavefield focusing using a generalised, potentially asymmetric homogeneous Green's function

Diekmann, Leon; Vasconcelos, Ivan; Wapenaar, Kees; Slob, Evert; Snieder, Roel

DOI
10.1016/j.wavemoti.2022.103071

Publication date
2023

Document Version
Final published version

Published in
Wave Motion

Wave Motion 116 (2023) 103071

Contents lists available at ScienceDirect

Wave Motion

journal homepage: www.elsevier.com/locate/wamot

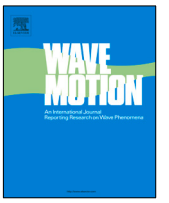

Wavefield focusing using a generalised, potentially asymmetric homogeneous Green's function

Leon Diekmann [a,*], Ivan Vasconcelos [a], Kees Wapenaar [b], Evert Slob [b], Roel Snieder [c]

[a] Utrecht University, Netherlands
[b] Delft University of Technology, Netherlands
[c] Colorado School of Mines, United States of America

ARTICLE INFO

Article history:
Received 8 April 2022
Received in revised form 2 September 2022
Accepted 28 September 2022
Available online 22 October 2022

Keywords:
Green's function
Inverse scattering
Focusing
Interferometry
Time reversal

ABSTRACT

Marchenko-type integrals typically relate so-called focusing functions and Green's functions via the reflection response measured on the open surface of a volume of interest. Originating from one dimensional inverse scattering theory, the extension to two and three dimensions set in motion various new developments regarding imaging in complex materials. This extension, however, is based on wavefield decomposition inside the volume and a truncated medium state, i.e. a version of the medium that is reflection-free underneath the focusing location, suggesting that evanescent, refracted and diving waves cannot be included in the representation. We elaborate on a new derivation for Marchenko-like integrals that (i) extends the concept of wavefield focusing by using a generalised homogeneous Green's function, (ii) is based on partial differential equations and thereby allows for additional insights and a new physical intuition for Marchenko equations, (iii) unifies wavefield focusing for open and closed boundary systems, (iv) does not require wavefield decomposition or a truncated medium state, thus including the full wavefield Green's function, (v) enables using forward modelling to obtain, e.g., Marchenko-type, time-compact focusing functions. We place a particular focus on the latter point, illustrating and investigating how to solve the underlying partial differential equations for various types of focusing functions. This paves the way for a deeper understanding of focusing functions as well as advanced full wavefield Marchenko schemes. While the derivations are generally presented for the 3D case, we show numerical examples in 1D.

1. Introduction

Inverse scattering theory [1,2] is a field of mathematical physics that aims to retrieve the physical properties of a medium based on its remotely observed scattering response to, e.g., acoustic, seismic or electro-magnetic waves. It is relevant to, for instance, quantum mechanics [3], optics [4], geophysics [5–7], medical imaging [8] and non-destructive testing [9]. The Marchenko integral is an essential equation in inverse scattering theory [10–12]. It is well defined in one dimension, where it can be used to directly infer the medium's scattering potential.

Following investigations of the focusing properties [13,14] of the Marchenko integral and its relation to the homogeneous Green's function [15,16], Wapenaar et al. [17,18] extended the concept to two and three dimensions. While

* Corresponding author.
E-mail address: l.d.diekmann@uu.nl (L. Diekmann).

https://doi.org/10.1016/j.wavemoti.2022.103071

the Marchenko scheme bears similarities with Green's function retrieval via conventional seismic interferometry [19–21], there are several, significant differences: (i) conventional interferometry allows to retrieve the response to a virtual source at the location of a physical receiver inside of a medium. The Marchenko scheme can be used to obtain the response to a virtual source anywhere in the medium without the need to have an actual, physical receiver at the target location [15]. (ii) Conventional interferometric relations involve solely Green's functions, whereas the Marchenko-type representations involve Green's and focusing functions. (iii) Conventional interferometry usually produces artefacts for open boundary (single-sided) representations because the underlying integral equation becomes approximate [22,23]. The Marchenko method on the other hand remains accurate even for open boundary integrals [24]. Hence, the extension of the Marchenko method to two and three dimensions paved the way for various new methodologies and applications, like Marchenko imaging [18], target-oriented imaging [25], multiple elimination [26,27] and monitoring [28,29]. While most of these applications are for acoustic waves, the Marchenko scheme was recently also extended to elastodynamic waves [30–33].

The extension of the Marchenko method to two and three dimensions also has some drawbacks. For complex, laterally varying media, i.e. inducing complicated wave scattering, the method tends to become unstable and may require further knowledge of the medium properties [34,35]. Furthermore, when using the method for Green's function retrieval one requires an estimate of the first arrival of the Green's function, e.g. from a smooth estimate of the actual medium [17]. In addition to these intrinsic limitations, it was until recently assumed that the representation would not include evanescent, refracted and diving waves in the Green's function. This was a consequence of the derivation relying on up-/down-decomposition of the wavefields inside the medium as well as a truncated medium state [18]. A first step towards including evanescent waves was made by Wapenaar [36]. Additionally, evanescent and refracted waves were studied in more detail [31,37]. Recently, a new derivation for a Marchenko-type equation was presented that circumvents these wavefield decomposition assumptions altogether, thus arguing that the Marchenko integral includes the full wavefield Green's function [38]. This derivation is different from previous approaches as it is based on a partial differential equation definition for focusing functions. Similar conclusions were presented by Wapenaar et al. [39], using a different derivation that is overall closer to previous strategies. Studies for closed boundary Marchenko-like schemes [40] also made the observation that up-/down-decomposition inside the medium is not a necessity [41].

In this paper we further extend, discuss and illustrate the novel approach to focusing functions [38,42]. We follow the original derivation in defining focusing functions by means of a partial differential equation and study the respective source terms in more detail. These source terms were only poorly understood before but play an essential role as they connect the focusing wavefields with the physical medium parameters. Being able to make this connection paves the way for, e.g., modelling reference focusing functions or setting up inversion methods to retrieve medium properties from given focusing functions. Above all, their investigation leads to a deeper understanding of focusing functions within this new framework, going beyond classical, Marchenko-type focusing functions. Based on this definition of focusing functions, we generalise the homogeneous Green's function [43], which represents a fundamental relation between anti-causal and causal field solutions, by presenting the so-called homogeneous Green's function of the second kind [38]. We illustrate and discuss these homogeneous Green's functions of the second kind, in particular their focusing properties and their relation to the conventional homogeneous Green's function. In this context we compare different classes of focusing functions, illustrated by numerical 1D examples. In particular, we investigate time-compact focusing functions for both double- and single-sided configurations. We use reciprocity theorems to derive Marchenko-like representations for both closed and open boundary integrals based on the underlying homogeneous Green's function of the second kind. These representations do not require any wavefield decomposition inside the medium, i.e. they deliver the full wavefield Green's function. While the numerical examples are in 1D, most of the theory is given for the general three dimensional case.

2. Focusing terminology

In this section we briefly discuss common terminology in the field of wave focusing. We consider this clarification important as we aim to connect different fields of research (that do not typically use the same terminology) in this paper. Conventionally, the term focus is used to describe a wavefield, e.g. pressure or particle velocity, that is concentrated around a certain point in space at a certain point in time [44]. In other words, if you take a snapshot of such a wavefield at the specific focusing time it will show a field that is collapsed to the area around the specific focusing point in space. The size of this focal area depends on the bandwidth of the wavefield — in the ideal case of infinite bandwidth it reduces to a point. We will refer to this as a focus in space. In time reversal acoustics, the process of injecting a wavefield into a medium in order to obtain such a focus in space is often referred to as time reversal focusing [45]. The incident wavefield that yields the focus is sometimes referred to as a focusing field, i.e. a field that focuses. When the Marchenko scheme was extended to 2D and 3D, the higher dimensional equivalents to solutions in classical 1D derivations [46] were named focusing functions [17]. By definition, these focusing functions are wavefields that collapse to a certain point in time at a certain point in space when injected into a truncated version of the actual medium from an open boundary [24]. Hence, if you pick the particular focusing point in space and look at the entire wavefield at this location over time it will exhibit what we will call a focus in time. We will illustrate the differences between focusing in space and time in Section 4. Furthermore, we want to stress that our definition of focusing functions in this paper as well as our reasoning for calling them such differs from previous work in the context of 2D and 3D Marchenko [17] but is consistent with time reversal acoustics. We will come back to these differences and explain their implications in Sections 3 and 4.

3. The homogeneous Green's function of the second kind

In this paper, we investigate acoustic waves in a lossless medium. Most of the concepts, however, in principle generalise to other partial differential equations, e.g. to the case of non-dissipative elastic media [47,48]. The acoustic wave equation is given by

$$\mathcal{L}(\boldsymbol{x})u(\boldsymbol{x},t) = -\rho(\boldsymbol{x})\frac{\partial}{\partial t}s(\boldsymbol{x},t) \quad , \tag{1}$$

with the acoustic wave operator

$$\mathcal{L}(\boldsymbol{x}) = \rho(\boldsymbol{x})\nabla\cdot\left(\frac{1}{\rho(\boldsymbol{x})}\nabla\right) - \frac{1}{c^2(\boldsymbol{x})}\frac{\partial^2}{\partial t^2} \quad , \tag{2}$$

where $u(\boldsymbol{x},t)$ is the pressure wavefield (in N/m^2) at location $\boldsymbol{x} = (x,y,z)$ and time t, $\rho(\boldsymbol{x})$ denotes mass density (in kg/m^3), $s(\boldsymbol{x},t)$ is a source term of volume injection rate density (in 1/s) and $c(\boldsymbol{x})$ is wave speed (in m/s). We define the Green's function $g(\boldsymbol{x},t;\boldsymbol{x_f})$ as the causal medium response in terms of acoustic pressure to an impulsive point source at location $\boldsymbol{x_f}$ and time zero [49], i.e.

$$\mathcal{L}(\boldsymbol{x})g(\boldsymbol{x},t;\boldsymbol{x_f}) = -\rho(\boldsymbol{x})\delta(\boldsymbol{x}-\boldsymbol{x_f})\frac{\partial}{\partial t}\delta(t) \quad . \tag{3}$$

Thus, the time-reversed Green's function $g(\boldsymbol{x},-t;\boldsymbol{x_f})$ obeys

$$\mathcal{L}(\boldsymbol{x})g(\boldsymbol{x},-t;\boldsymbol{x_f}) = \rho(\boldsymbol{x})\delta(\boldsymbol{x}-\boldsymbol{x_f})\frac{\partial}{\partial t}\delta(t) \quad . \tag{4}$$

Since we defined $g(\boldsymbol{x},t;\boldsymbol{x_f})$ as a causal field response, $g(\boldsymbol{x},-t;\boldsymbol{x_f})$ has to be anti-causal, i.e. it propagates prior to the associated source pulse at $t=0$. The homogeneous Green's function [43] is the superposition of the Green's function and the time-reversed Green's function, thus obeying

$$\mathcal{L}(\boldsymbol{x})\big(g(\boldsymbol{x},t;\boldsymbol{x_f}) + g(\boldsymbol{x},-t;\boldsymbol{x_f})\big) = 0 \quad . \tag{5}$$

The homogeneous Green's function is thus a source-free wavefield. Let us consider a bounded volume that contains $\boldsymbol{x_f}$ in a medium that is scattering-free outside the volume. The time-reversed, anti-causal Green's function is then purely in-coming with respect to that volume. It injects energy into the volume. The wavefield focuses at $\boldsymbol{x_f}$ and $t=0$ before propagating onwards as the out-going, causal Green's function.

We now establish the auxiliary focal solution $f\big(\boldsymbol{x},t;\boldsymbol{x_f},q(\boldsymbol{x},t)\big)$ as the causal wavefield that obeys

$$\mathcal{L}(\boldsymbol{x})f\big(\boldsymbol{x},t;\boldsymbol{x_f},q(\boldsymbol{x},t)\big) = \frac{\rho(\boldsymbol{x})\delta(\boldsymbol{x}-\boldsymbol{x_f})}{2}\frac{\partial}{\partial t}\delta(t) + q(\boldsymbol{x},t) \quad , \tag{6}$$

where the source function $q(\boldsymbol{x},t)$ is in principle arbitrary but is constrained to be symmetric in time, such that $q(\boldsymbol{x},t) = q(\boldsymbol{x},-t)$ [38,42]. In that sense, we can write any choice of a discrete source distribution $q(\boldsymbol{x},t)$ as a superposition of individual sources $q_i(\boldsymbol{x},t)$ according to

$$q(\boldsymbol{x},t) = \sum_{i=1}^{n} q_i(\boldsymbol{x},t) = \sum_{i=1}^{n} w_i\rho(\boldsymbol{x})\big(\delta(t-t_i)\star\mathfrak{s}_i(t) + \delta(t+t_i)\star\mathfrak{s}_i(-t)\big)\delta(\boldsymbol{x}-\boldsymbol{x}_i) \quad , \tag{7}$$

where n is the total number of terms that make up $q(\boldsymbol{x},t)$, w_i is a weighting factor, $\boldsymbol{x}_i$ and t_i are particular locations and times, respectively, $\mathfrak{s}_i(t)$ is an arbitrary wavelet and the $\star$ denotes convolution. The auxiliary focal solutions being causal means that for each source the energy emittance precedes the energy propagation through the volume — analogously to the definition of the Green's function. Hence, there might be propagating energy before $t=0$ due to sources in $q(\boldsymbol{x},t)$ at negative times. Note that the auxiliary focal solution can be expressed as

$$f\big(\boldsymbol{x},t;\boldsymbol{x_f},q(\boldsymbol{x},t)\big) = -\frac{1}{2}g(\boldsymbol{x},t;\boldsymbol{x_f}) + f_q\big(\boldsymbol{x},t;q(\boldsymbol{x},t)\big) \quad , \tag{8}$$

where $f_q\big(\boldsymbol{x},t;q(\boldsymbol{x},t)\big)$ is the causal medium response to the source distribution $q(\boldsymbol{x},t)$. The time-reversed auxiliary focal solution satisfies

$$\mathcal{L}(\boldsymbol{x})f\big(\boldsymbol{x},-t;\boldsymbol{x_f},q(\boldsymbol{x},t)\big) = -\frac{\rho(\boldsymbol{x})\delta(\boldsymbol{x}-\boldsymbol{x_f})}{2}\frac{\partial}{\partial t}\delta(t) + q(\boldsymbol{x},t) \quad . \tag{9}$$

As $f\big(\boldsymbol{x},t;\boldsymbol{x_f},q(\boldsymbol{x},t)\big)$ is purely causal, $f\big(\boldsymbol{x},-t;\boldsymbol{x_f},q(\boldsymbol{x},t)\big)$ is an anti-causal field. By subtracting Eq. (9) from Eq. (6) we get

$$\mathcal{L}(\boldsymbol{x})\Big(f\big(\boldsymbol{x},t;\boldsymbol{x_f},q(\boldsymbol{x},t)\big) - f\big(\boldsymbol{x},-t;\boldsymbol{x_f},q(\boldsymbol{x},t)\big)\Big) = \rho(\boldsymbol{x})\delta(\boldsymbol{x}-\boldsymbol{x_f})\frac{\partial}{\partial t}\delta(t) \quad . \tag{10}$$

Using Eq. (8) this can be written as

$$\mathcal{L}(\boldsymbol{x})\Big(-\frac{1}{2}g(\boldsymbol{x},t;\boldsymbol{x_f}) + \frac{1}{2}g(\boldsymbol{x},-t;\boldsymbol{x_f}) + f_q\big(\boldsymbol{x},t;q(\boldsymbol{x},t)\big) - f_q\big(\boldsymbol{x},-t;q(\boldsymbol{x},t)\big)\Big) = \rho(\boldsymbol{x})\delta(\boldsymbol{x}-\boldsymbol{x_f})\frac{\partial}{\partial t}\delta(t) \quad . \tag{11}$$

Note that Eqs. (10) and (11) involve the same wavefield — only the representation of the wavefield is different. The solution of this wave equation obeys the same source term as the time-reversed Green's function, Eq. (4). However, it is a fundamentally different wavefield. Firstly, it has both causal and anti-causal contributions. Secondly, it is non-unique, i.e. different choices of $q(\boldsymbol{x}, t)$ lead to different wavefields. Take for instance the trivial case $q(\boldsymbol{x}, t) = 0$, such that only the Green's functions remain. Eq. (11) can then be interpreted as describing a source that emits its energy in both time directions, backwards and forwards in time, governing both an anti-causal and a causal Green's function. As the wavefield propagates both forwards and backwards in time, each Green's function comes with a factor of 1/2. Alternatively, we can interpret the wavefields in the sense of purely increasing time as follows: consider a bounded volume that contains $\boldsymbol{x_f}$ in a medium that is scattering-free outside the volume. The time-reversed, half-amplitude Green's function is then purely in-coming with respect to that volume. The source acts as a sink and absorbs all of the in-coming energy. Furthermore, it emits additional energy into the medium, which then propagates forwards as the out-going, negative, half-amplitude Green's function. In the general case of $q(\boldsymbol{x}, t) \neq 0$ we additionally get the field contribution $f_q\big(\boldsymbol{x}, t; q(\boldsymbol{x}, t)\big) - f_q\big(\boldsymbol{x}, -t; q(\boldsymbol{x}, t)\big)$, which is source-free since the source distributions $q(\boldsymbol{x}, t)$ cancel each other — analogously to the homogeneous Green's function.

Because Eq. (10) has the same source term as the time-reversed Green's function, we can obtain a source-free field by adding the Green's function, i.e. we add Eq. (3) to get

$$\mathcal{L}(\boldsymbol{x})\Big(f\big(\boldsymbol{x}, t; \boldsymbol{x_f}, q(\boldsymbol{x}, t)\big) - f\big(\boldsymbol{x}, -t; \boldsymbol{x_f}, q(\boldsymbol{x}, t)\big) + g(\boldsymbol{x}, t; \boldsymbol{x_f})\Big) = 0 \quad . \tag{12}$$

We call the wavefield obeying Eq. (12) the homogeneous Green's function of the second kind. Just like the homogeneous Green's function in Eq. (5), the homogeneous Green's function of the second kind is a source-free wavefield that contains the causal Green's function. Note that adding the time-reversed of Eq. (12) to Eq. (12) gives the equation for the conventional homogeneous Green's function, Eq. (5). Consider a bounded volume that contains $\boldsymbol{x_f}$ in a medium that is scattering-free outside the volume. Furthermore, let $q(\boldsymbol{x}, t) = 0$ for all $\boldsymbol{x}$ outside the volume. The negative, time-reversed auxiliary focal solution $-f\big(\boldsymbol{x}, -t; \boldsymbol{x_f}, q(\boldsymbol{x}, t)\big)$ in Eq. (12) is then purely in-coming and injects energy into the volume. The resulting wavefield, after focusing or scattering, keeps on propagating as the out-going, causal auxiliary focal solution $f\big(\boldsymbol{x}, t; \boldsymbol{x_f}, q(\boldsymbol{x}, t)\big)$ and the out-going, causal Green's function. The homogeneous Green's function of the second kind always has a focus in space at $\boldsymbol{x_f}$ and $t = 0$ – because the only non-zero contribution to the wavefield at zero time stems from the Green's function. In that sense the negative, time-reversed auxiliary focal solution $-f\big(\boldsymbol{x}, -t; \boldsymbol{x_f}, q(\boldsymbol{x}, t)\big)$ is a focusing field. Just like the time-reversed Green's function in time reversal acoustics it can be injected into a source-free volume to create a focus in space, compare Section 2. The name *auxiliary focal solution* refers to the relation of these wavefields to focusing in space. From now on we will call $\phi\big(\boldsymbol{x}, t; \boldsymbol{x_f}, q(\boldsymbol{x}, t)\big) = -f\big(\boldsymbol{x}, -t; \boldsymbol{x_f}, q(\boldsymbol{x}, t)\big)$ a focusing function and $f\big(\boldsymbol{x}, t; \boldsymbol{x_f}, q(\boldsymbol{x}, t)\big)$ a negative, time-reversed focusing function. Note that the focusing function is an anti-causal field that focuses, whereas the negative, time-reversed focusing function is a causal field that expands.

As we already stated, our nomenclature – referring to the general fact that focusing functions are related to focusing in space – differs from the conventional reasoning, where the name was used for a specific type of function that is related to focusing in time [17]. We will later on find these previously introduced functions that focus in time to form a specific subset of our focusing functions.

We can use Eq. (8) to rewrite the homogeneous Green's function of the second kind as

$$\mathcal{L}(\boldsymbol{x})\Big(\frac{1}{2}g(\boldsymbol{x}, t; \boldsymbol{x_f}) + \frac{1}{2}g(\boldsymbol{x}, -t; \boldsymbol{x_f}) + f_q\big(\boldsymbol{x}, t; q(\boldsymbol{x}, t)\big) - f_q\big(\boldsymbol{x}, -t; q(\boldsymbol{x}, t)\big)\Big) = 0 \quad , \tag{13}$$

highlighting the similarity with the conventional homogeneous Green's function. This representation shows that the homogeneous Green's function of the second kind can in fact be written as a superposition of symmetric and anti-symmetric wavefields in time. The representation in Eq. (12) on the other hand underlines the potentially asymmetric appearance in time of the homogeneous Green's function of the second kind.

Of course one can also construct other homogeneous wavefields in a similar fashion, e.g.

$$\mathcal{L}(\boldsymbol{x})\Big(f\big(\boldsymbol{x}, t; \boldsymbol{x_f}, q(\boldsymbol{x}, t)\big) - f\big(\boldsymbol{x}, -t; \boldsymbol{x_f}, q(\boldsymbol{x}, t)\big) - g(\boldsymbol{x}, -t; \boldsymbol{x_f})\Big) = 0 \quad , \tag{14}$$

i.e. by combining focusing and Green's functions. We will, however, focus our discussion in this paper on the homogeneous Green's function of the second kind in Eq. (12).

In this section we introduced focusing functions. Such focusing functions allow for the construction of the homogeneous Green's function of the second kind, Eq. (12). All important wavefields are also sketched in Fig. 1. In the next section we discuss and illustrate different focusing functions.

4. Examples of focusing functions

In this section we discuss different focusing functions — with the objective of illustrating how our partial differential equation scheme represents physical focusing wave-states including (but not limited to) those obtainable by previous approaches. In that sense, some of the upcoming examples represent entirely new focusing wave states that can only now be investigated by studying source terms $q(\boldsymbol{x}, t)$ in our new framework. All focusing functions have a fundamental, unifying property: when superimposing the corresponding homogeneous Green's functions of the second kind and their time-reversed counterparts one always obtains the conventional homogeneous Green's functions. This implies that the

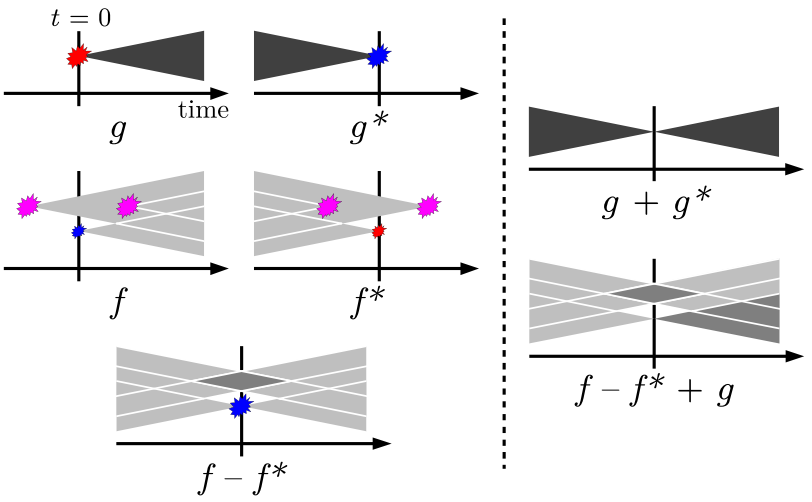

Fig. 1. Illustration of different wavefield causalities. Cones that open to the right are causal, cones that open to the left are anti-causal. The $*$ denotes time-reversed wavefields. Axis are labelled only in the top left sketch for the sake of a cleaner figure. Wavefields with sources are shown to the left of the dotted vertical line, source-free wavefields are shown to the right of the line. The red and blue explosions denote the source terms related to the Green's function and the time-reversed – opposite sign – Green's function, respectively, where the size of the symbol correlates with the source magnitude. The pink explosions mark the source distribution $q(\boldsymbol{x}, t)$. Dark grey cones are related to Green's functions, light grey cones to auxiliary focal solutions. The medium grey colour indicates interference of either forward and time-reversed auxiliary focal solutions or auxiliary focal solutions and Green's functions. Note that the vertical shift of the pink sources compared to the sources of the Green's functions is arbitrary, solely indicating a potentially different location in space. (For interpretation of the references to colour in this figure legend, the reader is referred to the web version of this article.)

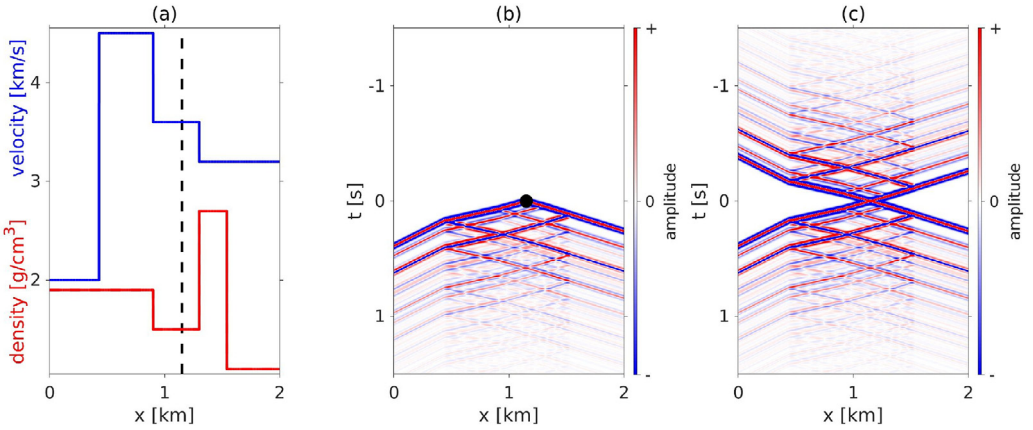

Fig. 2. (a) Velocity and density model in blue and red, respectively. The black dotted line marks the focusing location $x_f = 1.15$ km. (b) Green's function. The black dot denotes the focusing location, i.e. source location, at $x_f = 1.15$ km and $t = 0$ s. (c) Homogeneous Green's function. The colour bars in (b) and (c) are clipped at about 14 % of the maximum absolute value of the Green's function. (For interpretation of the references to colour in this figure legend, the reader is referred to the web version of this article.)

homogeneous Green's functions of the second kind always have a single delta pulse at the focusing location $\boldsymbol{x_f}$ and are zero elsewhere at zero time, i.e. the wavefields focus in space. This will also become evident in the examples below.

Despite this property, focusing functions vary significantly in appearance. We discuss four groups in the following: focusing functions for the trivial choice $q(\boldsymbol{x}, t) = 0$, functions with a simple monopole source, with a simple dipole source, and time-compact focusing functions. The initial, simple examples are used to illustrate fundamental properties of focusing functions and explain how we can enforce interesting interference patterns within the fields. Based on these concepts we can then construct more complex, time-compact focusing functions. The numerical examples are in 1D to allow for optimum illustrations. The concepts that we discuss, however, are not necessarily limited to 1D, although more elaborate schemes might be necessary for higher dimensional investigations, incorporating, e.g., angle-dependent reflectivity and geometrical spreading. In 1D the spatial coordinate $\boldsymbol{x}$ becomes the scalar x, e.g. the focusing location reads x_f.

The numerical examples are based on the velocity and density model in Fig. 2(a) and consider the point $x_f = 1.15$ km. As a reference for later results, Fig. 2(b) shows the Green's function for $x_f = 1.15$ km, obtained via finite difference

modelling according to Eq. (3). Note that all wavefields that we show in this paper are convolved with a 20 Hz Ricker wavelet [50] for improved visualisation. Furthermore, all wavefields are clipped at the same amplitudes as Fig. 2(b) to allow for a good comparison. Owing to the orientation of the spatial axis in this plot we will refer to leftwards and rightwards travelling events in space. Note, however, that in multiple dimensions it is also common to differentiate between up- and down-going waves in space, corresponding to left- and right-going waves, respectively, in our 1D figures. Fig. 2(c) gives the respective homogeneous Green's function, obtained by superimposing the field in Fig. 2(b) and its time-reversed version. Alternatively, the homogeneous Green's function could be obtained by injecting the time-reversed Green's function from the boundary ∂V, i.e. from $x = 0$ km and $x = 2$ km, into the source-free medium. This process is referred to as time reversal acoustics [45,51]. Using reciprocity and a radiation condition [19] to get the respective equivalent sources, the homogeneous Green's function then follows for $\boldsymbol{x}$ in V by modelling according to

$$\mathcal{L}(\boldsymbol{x})\big(g(\boldsymbol{x}, t; \boldsymbol{x_f}) + g(\boldsymbol{x}, -t; \boldsymbol{x_f})\big) = -\int_{\boldsymbol{x_r}\in\partial V} \frac{2}{c(\boldsymbol{x_r})}\delta(\boldsymbol{x}-\boldsymbol{x_r})\frac{\partial}{\partial t} g(\boldsymbol{x_r}, -t; \boldsymbol{x_f})\, d\boldsymbol{S} \quad , \tag{15}$$

where we assume that V contains $\boldsymbol{x_f}$ and that the medium is reflection-free outside V [52,53]. However, this modelled homogeneous Green's function might be numerically less accurate than the one we obtain from superimposing the Green's function and its time-reversed version. This is due to the fact that the Green's function generally is a time-infinite field response, i.e. even at very large recording times one might still record multiple scattered events. Consequently, we would have to record the Green's function until the amplitudes of these late arrivals become negligible — otherwise the Green's function is missing energy and injecting its time-reversed version into the medium will not accurately reproduce the homogeneous Green's function. In our numerical example we still have considerable events at 1.5 s, i.e. at the end of the recorded data. Therefore, we choose not to use modelling with Eq. (15) in order to obtain the best quality reference homogeneous Green's function. Fig. 2(c) shows the focus in space of the homogeneous Green's function at $t = 0$. Note that owing to the symmetry of the wavefield, the time derivative of the displayed pressure field is zero.

For the homogeneous Green's functions of the second kind on the other hand, we do use time reversal modelling with the goal of actually illustrating the wave propagation through the source-free medium. Similar to Eq. (15) we then obtain for $\boldsymbol{x}$ in V

$$\mathcal{L}(\boldsymbol{x})\Big(f\big(\boldsymbol{x}, t; \boldsymbol{x_f}, q(\boldsymbol{x}, t)\big) - f\big(\boldsymbol{x}, -t; \boldsymbol{x_f}, q(\boldsymbol{x}, t)\big) + g(\boldsymbol{x}, t; \boldsymbol{x_f})\Big) = \int_{\boldsymbol{x_r}\in\partial V} \frac{2}{c(\boldsymbol{x_r})}\delta(\boldsymbol{x}-\boldsymbol{x_r})\frac{\partial}{\partial t} f\big(\boldsymbol{x_r}, -t; \boldsymbol{x_f}, q(\boldsymbol{x}, t)\big)\, d\boldsymbol{S} \quad , \tag{16}$$

where we assume that the medium is reflection-free outside the bounded volume as well as that V contains $\boldsymbol{x_f}$. While the source distribution is arbitrary within V, we assume $q(\boldsymbol{x}, t) = 0$ for all $\boldsymbol{x}$ outside V, such that $-f\big(\boldsymbol{x_r}, -t; \boldsymbol{x_f}, q(\boldsymbol{x}, t)\big)$ is the only in-coming wavefield.

4.1. Trivial focusing functions

First, we consider the trivial, negative, time-reversed focusing function $f(x, t; x_f) = -1/2\, g(x, t; x_f)$ for $q(x, t) = 0$, as shown in Fig. 3(a). Compared to the Green's function in Fig. 2(b) the polarity is reversed and the amplitudes are divided by two. According to Eq. (13) the homogeneous Green's function of the second kind equals the conventional homogeneous Green's function divided by two in this case. In a way, the conventional homogeneous Green's function can therefore be considered a special case of the homogeneous Green's function of the second kind. For $q(x, t) = 0$ Eq. (16) gives Eq. (15). Modelling the homogeneous Green's function of the second kind accordingly, i.e. emitting the focusing function from the boundaries $x = 0$ km and $x = 2$ km into the medium, delivers the wavefield in Fig. 3(b). It is similar to the homogeneous Green's function in Fig. 2(c), but the amplitudes differ by a factor of two. The grey polygon in Fig. 3(b) on the top, i.e. above -1 s, denotes the area of the data that is unaffected by the injected wavefield — this is a consequence of causality, as it takes time for the injected wavefield to travel from the injection boundaries to the interior of the volume. The lower grey polygon is its time-reversed version. As we know that the wavefield in Fig. 3(b) should be symmetric in time (being the half amplitude homogeneous Green's function), we should have the same solution in both polygons, suggesting that the wavefield should be zero within the lower grey polygon — which is not quite the case in this example. This is why, as mentioned before, time reversal modelling tends to be inaccurate for short recording times. Finally, Fig. 3(c) shows the homogeneous Green's function, obtained by superimposing the wavefield in Fig. 3(b) and its time-reversed version. This wavefield is indeed a reasonable estimate of the homogeneous Green's function in Fig. 2(c).

4.2. Focusing functions with a monopole source

Let us consider $q(x, t)$ with a single term, i.e. $n = 1$ in Eq. (7). We discuss two different choices for $s_1(t)$ in the following.

First, we consider the simple case $s_1(t) = -\delta(t)$. Furthermore, we use $x_1 = 1$ km and $t_1 = 0.17$ s for this example. The weighting term w_1 is chosen such that the amplitude of the resulting signal is a quarter of that of the Green's function. Fig. 3(d) shows the negative, time-reversed focusing function, obtained by forward modelling via Eq. (6). Since the additional source term $q(x, t)$ does not contain a time derivative, the resulting signal appears to be convolved with a 20 Hz Ricker wavelet that was integrated over time, i.e. its wavelet does not match the wavelet of the Green's function. When injecting the focusing function into the medium via Eq. (16) we get the homogeneous Green's function of the second

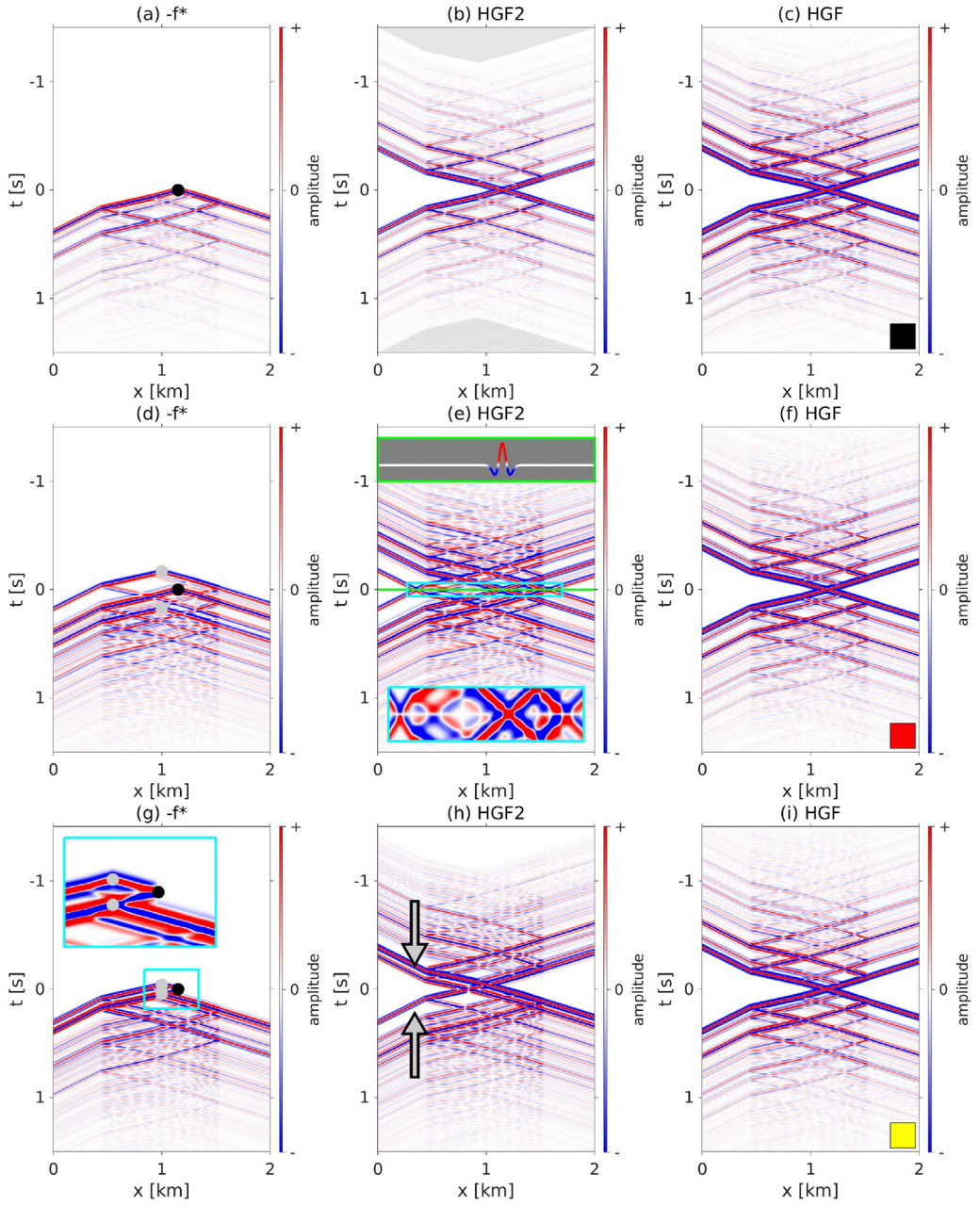

Fig. 3. Left column: negative, time-reversed focusing functions (abbreviated with $-f^*$ in the title) obtained from finite difference modelling with Eq. (6). Black dots mark the locations of the Green's function source at x_f, grey dots the locations of the source distributions $q(x,t)$ and $q(x,t;x_f)$, respectively. Central column: homogeneous Green's functions of the second kind (*HGF*2 in the title), obtained via modelling according to Eq. (16). Right column: homogeneous Green's functions (*HGF* in the title) obtained by superimposing the homogeneous Green's functions of the second kind and their time-reversed versions. The coloured squares in the bottom right corners refer to Fig. 7. (a), (b) and (c) are for $q(x,t)=0$. (d), (e) and (f) are for a monopole $q(x,t)$ without time derivative. (g), (h) and (i) are for a monopole $q(x,t;x_f)$ with a time derivative. Zoomed regions are denoted by cyan windows. The trace in the green window shows the wavefield in (e) at time zero. (For interpretation of the references to colour in this figure legend, the reader is referred to the web version of this article.)

kind in Fig. 3(e). This wavefield differs from the conventional homogeneous Green's function. At $t=0$, the wavefield is only non-zero at the focusing location x_f – there are, however, various other events in space right before and after $t=0$. These events are related to the portion of the wavefield that is anti-symmetric in time. In the zoomed area (cyan box), one can see that these events change polarity when comparing negative and positive times and are zero at zero time. The only actual event at zero time is the focus at $x_f = 1.15$ km, i.e. the field exhibits a focus in space. This focus can also be seen in the green box, showing the wavefield at time zero. Note, however, that the derivative of the wavefield in

Fig. 3(e) is different from zero, leading to a significantly different appearance of the focusing compared to Fig. 2(c). When adding the homogeneous Green's function of the second kind and its time-reversed version we obtain the conventional homogeneous Green's function, see Fig. 3(f). The Green's function that was previously polluted by the signal of the source distribution $q(x,t)$, see Fig. 3(d), is now isolated. This is a result of the fact that the Green's functions in Eq. (13) are symmetric in time, while the fields $f_q\big(x,t;q(x,t)\big)$ are anti-symmetric in time.

The second option we present is $\mathfrak{s}_1 = -\partial\delta(t)/\partial t$, leading to

$$q(x,t;x_f) = w_1\rho(x)\left(-\frac{\partial}{\partial t}\delta(t-t_1)+\frac{\partial}{\partial t}\delta(t+t_1)\right)\delta(x-x_1) \quad . \tag{17}$$

This produces a wavelet similar to that of the Green's function, enabling a potentially interesting interference of the two terms $-1/2\,g(x,t;x_f)$ and $f_q\big(x,t;q(x,t)\big)$ within the negative, time-reversed focusing function, see Eq. (8). Note that this interference is only possible for $t_1 \neq 0$, because for $t_1 = 0$ we get $q(x,t) = 0$, leading to the trivial focusing function. Since this source distribution is supposed to interfere with the source at x_f, we write $q(x,t;x_f)$ here rather than $q(x,t)$. Note that the source distribution then generally also depends on the physical properties of the medium. We choose $x_1 = 1$ km, such that x_1 is in the same layer as x_f. Then we use $t_1 = (x_f - x_1)/c_3$, where c_3 is the velocity in this, i.e. the third, layer. On choosing $w_1 = -1/2$ we get a source at $t = -t_1$ that leads to destructive interference with the rightwards travelling portion of the negative, half-amplitude Green's function, see Fig. 3(g). As a consequence, it seems as if the source at x_f was only radiating energy to the left. The respective homogeneous Green's function of the second kind is shown in Fig. 3(h). While the previous homogeneous Green's functions of the second kind clearly revealed a superposition of perfectly symmetric and anti-symmetric fields in time, Fig. 3(h) is asymmetric in time. The grey arrows point to an event in the left part of the model that is present at negative but missing at positive times. This asymmetry is a consequence of the interference of $-1/2\,g(x,t;x_f)$ and $f_q\big(x,t;q(x,t;x_f)\big)$ within the negative, time-reversed focusing function. Such an interference would also be possible if x_1 was not in the same layer as the source of the Green's function, however, it would require an adjusted scaling value w_1. The respective conventional homogeneous Green's function, obtained by summing the wavefield in Fig. 3(h) and its time-reversed, can be seen in Fig. 3(i).

While the first example illustrated the effect of a simple, random source term, the second example nicely showed that we can produce interesting, destructive interference by applying particularly designed sources.

4.3. Focusing functions with a dipole source

In the previous subsection, we argued that a monopole source $q(x,t;x_f)$ with a time derivative at x_1 and $t_1 = 0$ cannot interfere with the signal of the negative half-amplitude Green's function, but only delivers the trivial focusing function. Dipole sources on the other hand do not have such a limitation. Regarding the 1D version of Eq. (7) we use $n = 1$ and $\mathfrak{s}_1(t) = -c(x_1)\delta(t)\partial/\partial x$ — note that $\mathfrak{s}_1(t)$ is a function of only the variable t but includes a spatial derivative. The source term therefore becomes

$$q(x,t;x_f) = -w_1\rho(x)c(x_1)\big(\delta(t-t_1)+\delta(t+t_1)\big)\frac{\partial}{\partial x}\delta(x-x_1) \quad . \tag{18}$$

We stress that the velocity $c(x_1)$ represents scaling with a particular velocity, i.e. at x_1, whereas the density $\rho(x)$ is a function under the action of the spatial Dirac delta. This becomes important later on when considering dipole sources at interfaces. This source produces a wavelet similar to that of the Green's function, but without delivering a trivial homogeneous Green's function of the second kind for $t_1 = 0$. In our finite difference code, we mimic the dipole source by two monopole sources with opposite polarity. We illustrate two different choices for the source time t_1 in the following, i.e. $t_1 \neq 0$ and $t_1 = 0$.

For the first numerical example we use the values from the preceding experiment, that is $x_1 = 1$ km, $t_1 = (x_f - x_1)/c_3$ and $w_1 = -1/2$, see Fig. 4(a). The resulting negative, time-reversed focusing function is similar to that in Fig. 3(g), only the polarities of some events appear reversed. Note that the two monopole sources in Fig. 3(g) that are associated with $q(x,t;x_f)$ have different polarities, while the two dipole sources in Fig. 4(a) exhibit the same polarity. The character of the homogeneous Green's function of the second kind follows our previous observations, i.e. Fig. 4(b) is slightly asymmetric, see grey arrows. Summing this wavefield and its time-reversed version gives the conventional homogeneous Green's function in Fig. 4(c).

Next, let us consider the case $t_1 = 0$. In order for $-1/2\,g(x,t;x_f)$ and $f_q\big(x,t;q(x,t;x_f)\big)$ to interfere destructively, we choose $x_1 = x_f$ and $w_1 = 1/4$ (note that the source is fired twice in Eq. (18)). The negative, time-reversed focusing function is shown in Fig. 4(d). It appears the source at x_f now only emits energy to the right. There are no additional, polluting signals from the $q(x,t;x_f)$ source — instead, its wavefield masks the left-going Green's function. Thus, the remaining wavefield represents the negative, right-going part of the Green's function, i.e. all its contributions that travel into greater depth first. The homogeneous Green's function of the second kind, Fig. 4(e), thus shows the time-reversed, positive, right-going part of the Green's function first, i.e. at negative times, followed by the positive, left-going part. Note that the scaling matches that of the actual Green's function. By adding left- and right-going parts, i.e. adding the homogeneous Green's function of the second kind and its time-reversed version, we obtain the conventional homogeneous Green's function, Fig. 4(f).

The first dipole experiment demonstrated how to achieve destructive interference similar to that in the previous subsection, however, the source signatures are now obviously different. The second example illustrated destructive interference generated by a source at zero time, an effect that can only be produced with dipole sources.

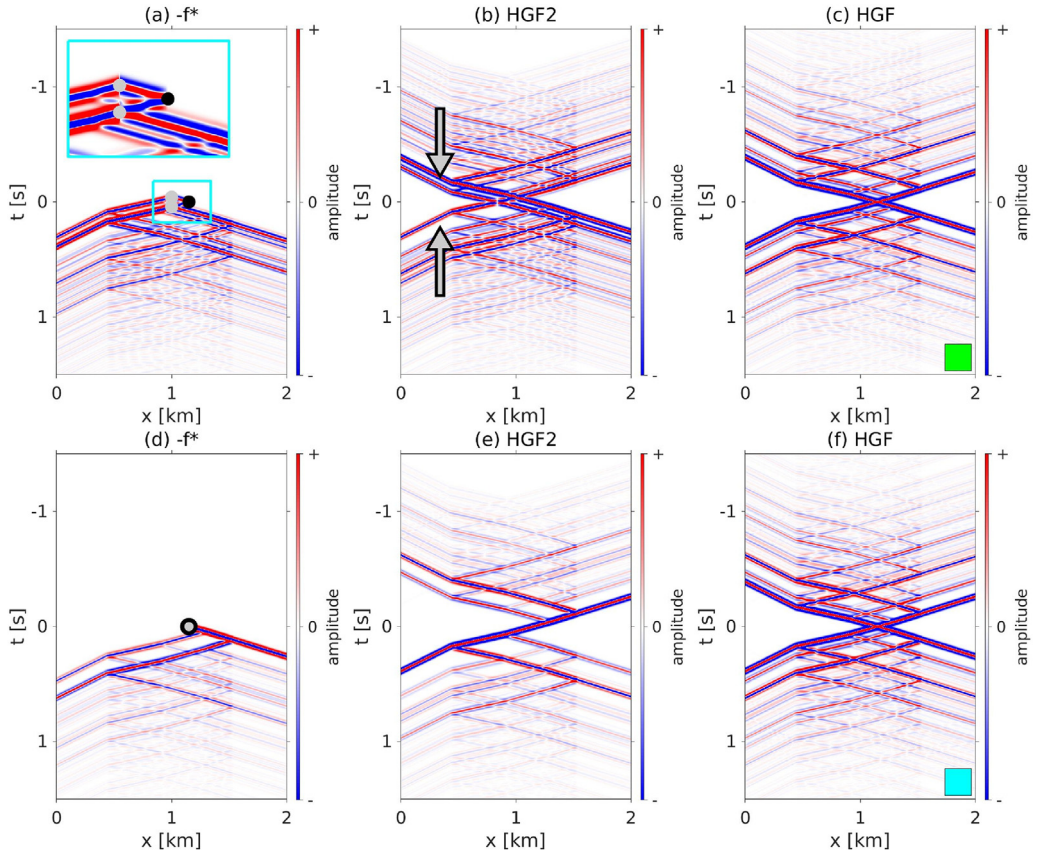

Fig. 4. Left column: negative, time-reversed focusing functions. Black dots mark the locations of the Green's function source at x_f, grey dots the locations of the $q(x, t; x_f)$ sources. Central column: homogeneous Green's functions of the second kind. Right column: homogeneous Green's functions obtained from the homogeneous Green's functions of the second kind. (a), (b) and (c) are for the dipole $q(x, t; x_f)$ related to $t_1 \neq 0$. (d), (e) and (f) are for the dipole $q(x, t; x_f)$ related to $t_1 = 0$. Zoomed regions are denoted by cyan windows. (For interpretation of the references to colour in this figure legend, the reader is referred to the web version of this article.)

4.4. Time-compact focusing functions

In the preceding subsections we introduced source distributions $q(x, t; x_f)$ that excite wavefields that interfere with the Green's function. Since dipole sources appear to be slightly more flexible than monopole sources, i.e. choosing $t_i = 0$ does not deliver a trivial focusing function, we use solely $s_i(t) = -c(x_i)\delta(t)\partial/\partial x$ in this subsection. Building on the findings described above, we illustrate and discuss particularly interesting wavefields in the following, i.e. so-called time-compact focusing functions. As the name suggests, these focusing functions occupy only a limited window in time, meaning that the wavefields are zero outside a certain time range. In contrast, Green's functions are generally time-infinite wavefields that keep on propagating for arbitrarily long time and it is only owing to their decreasing amplitude with each scattering interaction that we can usually neglect late arrivals. The time-compact focusing functions in this section relate to auxiliary focal solutions in classical 1D inverse scattering theory [11] and to the previously introduced subset of focusing functions in 2D and 3D Marchenko [18].

We propose a simple scheme for designing these time-compact focusing functions, consisting of two main steps: (i) get all space and time coordinates x_i and t_i, (ii) set up a linear system of equations to describe the scattering and obtain the weights w_i. Then, we can model the negative, time-reversed focusing functions via Eqs. (6) and (7). We present three different time-compact focusing functions below.

4.4.1. Double-sided sources at zero time

In order to design a time-compact focusing function, we first have to specify either the time or the space coordinates of the sources. The easiest approach is to assume that all sources in the distribution $q(x, t; x_f)$ are at $t_i = 0$ (implying a necessity for dipole sources). Furthermore, we assume that the sources may be anywhere in space, i.e. above and below x_f, thus we refer to this example as double-sided. For the negative, time-reversed focusing function (and consequently the focusing function) to be time-compact, each reflection of $-1/2\, g(x, t; x_f)$ in Eq. (8) has to be cancelled by a source in

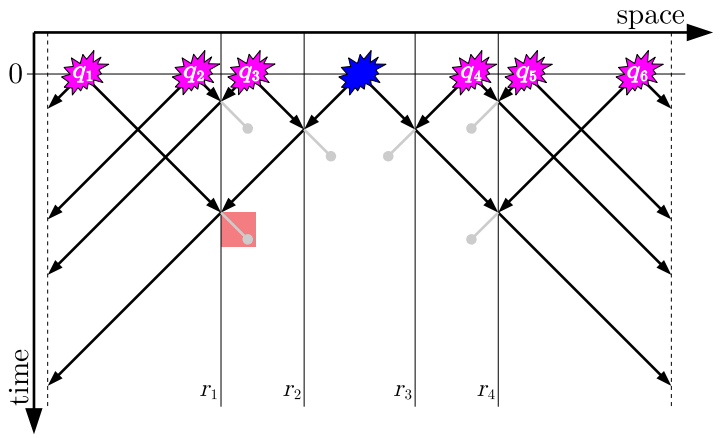

Fig. 5. Sketch of the time-compact, time-reversed focusing function using double-sided sources at zero time in a five layer medium. The reflection coefficient r_1 marks the first, r_2 the second, r_3 the third and r_4 the fourth interface. The blue explosion refers to the source of the negative, half-amplitude Green's function at x_f. The pink explosions denote the source distribution $q(x, t; x_f)$. Note that each $q_i(x, t; x_f)$ in this sketch actually represents two overlapping sources, compare Eq. (7). The black arrows represent propagating events, the grey lines imply reflections which are suppressed in the time-compact focusing function. The red square marks a region of interest which is studied in detail in the text. Note that the arrows in this sketch are straight for the sake of simplicity, but the wave speed in the different layers might actually vary. (For interpretation of the references to colour in this figure legend, the reader is referred to the web version of this article.)

$q(x, t; x_f)$, compare Fig. 5. Thus, when choosing $t_i = 0$ for all $n = 6$ sources in $q(x, t; x_f)$, we can compute the coordinates x_i that allow for a possible interference via ray tracing or, in the example on hand, simple travel time considerations. The source $q_1(x, t; x_f)$ for instance has to cancel the first reflection of the negative, half-amplitude Green's function at the first interface. Hence, the wave emitted from $q_1(x, t; x_f)$ should reach the first interface at the same time as the first arrival of the Green's function. The source $q_3(x, t; x_f)$ is supposed to cancel the first reflection of the negative, half-amplitude Green's function at the second interface. The wave emitted from $q_3(x, t; x_f)$ should therefore reach the second interface at the same time as the first arrival of the Green's function. The source $q_2(x, t; x_f)$ on the other hand has to eliminate the reflection at the first interface that is induced by the wavefield from $q_3(x, t; x_f)$. The wave emitted from $q_2(x, t; x_f)$ should consequently reach the first interface at the same time as the first arrival of the wave coming from $q_3(x, t; x_f)$. Similar considerations hold for the remaining sources. Overall, this gives the following space coordinates:

$$x_1 = \xi_1 - \left(\frac{x_f - \xi_2}{c_3} + \frac{\xi_2 - \xi_1}{c_2}\right)c_1 \tag{19}$$

$$x_2 = \xi_1 - \frac{x_3 - \xi_1}{c_2}c_1 \tag{20}$$

$$x_3 = \xi_2 - \frac{x_f - \xi_2}{c_3}c_2 \tag{21}$$

$$x_4 = \xi_3 + \frac{\xi_3 - x_f}{c_3}c_4 \tag{22}$$

$$x_5 = \xi_4 + \frac{\xi_4 - x_4}{c_4}c_5 \tag{23}$$

$$x_6 = \xi_4 + \left(\frac{\xi_3 - x_f}{c_3} + \frac{\xi_4 - \xi_3}{c_4}\right)c_5 \quad , \tag{24}$$

where ξ_j with $j = 1, 2, 3, 4$ is the location of the jth interface of our five layer model and c_k with $k = 1, 2, 3, 4, 5$ is the velocity in the kth layer. Note that we assume that $x_3 > \xi_1$ and $x_4 < \xi_4$ in our considerations. In other words we assume that $q_3(x, t; x_f)$ is located in the second layer and $q_4(x, t; x_f)$ in the fourth layer. Depending on the medium velocities, $q_3(x, t; x_f)$ could also fall within the first layer and $q_4(x, t; x_f)$ within the last, meaning that the sources $q_2(x, t; x_f)$ and $q_5(x, t; x_f)$ would become unnecessary and the coordinate calculations for x_3 and x_4 would change. The overall concept, however, remains the same. In addition, we assume that the sources lie within the layers, not at interfaces.

Now we know the space and time coordinates of the sources, but we still need to find out the six weights w_i. Note that we also have six equations, i.e. one for each grey line in Fig. 5 where a reflected wave is supposed to be cancelled. Let us consider the point marked by the red square in Fig. 5. There are three different events that reach this point: the negative, half-amplitude Green's function is transmitted at the second and reflected at the first interface, its amplitude is proportional to $\rho(x_f)c(x_f)r_1(1 - r_2)/2$, where $r_j = (\rho_{j+1}c_{j+1} - \rho_j c_j)/(\rho_{j+1}c_{j+1} + \rho_j c_j)$ is the reflection coefficient of the jth interface. Note that its actual amplitude corresponds to $\rho(x_f)c(x_f)r_1(1 - r_2)/4$ – the additional factor of 1/2, however,

turns up for all sources and is thus contained in the proportionality factor here. The wave from $q_3(x, t; x_f)$ is reflected at both the second and the first interface, its amplitude is therefore proportional to $r_1 r_2 2\rho(x_3)c(x_3)w_3$. Note that we use dipole sources $q_i(x, t; x_f)$ that emit leftwards with positive and rightwards with negative amplitude for positive weights w_i. Furthermore, it is important to remember that there are two sources in each $q_i(x, t; x_f)$ in Eq. (7), one at positive and one at negative time — hence, we get the factor of two. The wave from $q_1(x, t; x_f)$ is transmitted at the first interface and has an amplitude proportional to $-(1 + r_1)2\rho(x_1)c(x_1)w_1$. Thus we get the equation

$$-(1 + r_1)\rho(x_1)c(x_1)w_1 + r_1 r_2 \rho(x_3)c(x_3)w_3 = -\frac{\rho(x_f)c(x_f)}{2}\frac{r_1(1 - r_2)}{2} \quad , \tag{25}$$

which states that the events should cancel each other out. Repeating this procedure for the areas denoted by the five other grey lines in Fig. 5 we get the following linear system

$$\begin{bmatrix} -(1+r_1) & 0 & r_1 r_2 & 0 & 0 & 0 \\ 0 & -(1+r_1) & -r_1 & 0 & 0 & 0 \\ 0 & 0 & -(1+r_2) & 0 & 0 & 0 \\ 0 & 0 & 0 & 1-r_3 & 0 & 0 \\ 0 & 0 & 0 & -r_4 & 1-r_4 & 0 \\ 0 & 0 & 0 & -r_3 r_4 & 0 & 1-r_4 \end{bmatrix} \begin{bmatrix} \rho(x_1)c(x_1) \\ \rho(x_2)c(x_2) \\ \rho(x_3)c(x_3) \\ \rho(x_4)c(x_4) \\ \rho(x_5)c(x_5) \\ \rho(x_6)c(x_6) \end{bmatrix} \circ \begin{bmatrix} w_1 \\ w_2 \\ w_3 \\ w_4 \\ w_5 \\ w_6 \end{bmatrix} = \frac{\rho(x_f)c(x_f)}{2} \begin{bmatrix} -r_1(1-r_2)/2 \\ 0 \\ -r_2/2 \\ r_3/2 \\ 0 \\ (1+r_3)r_4/2 \end{bmatrix} \quad , \tag{26}$$

where $\circ$ is the Hadamard product. The determinant of the matrix is $(r_1+1)^2(r_2+1)(r_3-1)(r_4-1)^2$ which is different from zero for all reflection coefficients $|r_j| < 1$ with $j = 1, 2, 3, 4$, thus its inverse exists for all physically reasonable scenarios. We can solve the above system of equations to obtain the weights w_i and then model the negative, time-reversed focusing function via Eq. (6), where each of the $n = 6$ sources in Eq. (7) is given by

$$q_i(x, t; x_f) = -2w_i\rho(x)c(x_i)\delta(t)\frac{\partial}{\partial x}\delta(x - x_i) \quad . \tag{27}$$

The accordingly modelled negative, time-reversed focusing function is shown in Fig. 6(a). This wavefield is indeed only propagating between $t = 0$ s and about $t = 0.4$ s. Afterwards, there is no more energy travelling within the bounded volume between $x = 0$ km and $x = 2$ km. Note that this negative, time-reversed focusing function (and consequently the focusing function) is focused in time, i.e. at $x = x_f$ the field is only non-zero at $t = 0$. This is the eponymous focusing property of focusing functions in previous Marchenko literature [17]. In the context of our theory, however, only particular focusing functions, i.e. those which are compact in time, have such a focus in time — all focusing functions, however, can be related to a focus in space via the homogeneous Green's function of the second kind. Thus, these previously introduced functions form a subgroup of focusing functions in our framework.

The homogeneous Green's function of the second kind is given in Fig. 6(b). The asymmetry of the field is much more pronounced than before, as the wavefield is in fact zero before about -0.4 s but it keeps on propagating for infinitely long at positive times. This suggests that time reversal modelling is more accurate when using such a time-compact focusing function instead of, e.g., a time-reversed Green's function, because we do not need long recording times of the injected wavefield to achieve high accuracy. In contrast, we only need about 0.4 s of data. Let us define the data misfit as $\int\int \left(d(x, t; x_f) - d_{est}(x, t; x_f)\right)^2 dt\, dx$, where $d(x, t; x_f) = g(x, t; x_f) + g(x, -t; x_f)$ is the ground truth in Fig. 2(c) and $d_{est}(x, t; x_f)$ its estimate from the respective focusing function. Indeed, we find this data misfit to be significantly smaller for the new homogeneous Green's function, Fig. 6(c), than that for Fig. 3(c). This can also be seen in Fig. 7. While there is a significant misfit for all of the five preceding experiments, it is nearly zero for the time-compact focusing function. Note that if we had used larger recording times (greater than 1.5 s) for the previous experiments, the misfits would have appeared smaller in Fig. 7 – however, it would have been a subjective task to decide where to stop the recording in these scenarios whereas it is immediately clear with the time-compact focusing function that only requires a finite recording time of about 0.4 s in this example.

While this source setup works fairly well and is relatively straightforward, there is only one issue: in order for $q(x \notin V, t; x_f) = 0$ to hold, the respective volume V has to be relatively large. This can be seen in Fig. 5, where $q_1(x, t; x_f)$, $q_2(x, t; x_f)$, $q_5(x, t; x_f)$ and $q_6(x, t; x_f)$ are beyond the actual scattering region, i.e. the area bounded by the first interface r_1 on the left and the last interface r_4 on the right. For many experimental setups, however, it is desirable to consider only a smaller volume, limited to the actual scattering region, such that the volume does not have to be homogeneously extended beyond the first and last interface. Thus, it might make sense to think about other configurations.

4.4.2. Double-sided sources at the interfaces

Rather than picking times t_i for the source coordinates first, we can also pick locations x_i instead. In this context it might make sense to refer to the model features, i.e. we can put the sources at the interfaces between the five layers. We still keep the setup such that sources can be both above and below x_f. Hence, we now discuss double-sided sources at the interfaces. As before, each reflection of $-1/2\, g(x, t; x_f)$ in Eq. (8) has to be cancelled by a source in $q(x, t; x_f)$, see Fig. 8(a). Thus, we have $x_1 = \xi_1$, $x_2 = \xi_1$, $x_3 = \xi_2$, $x_4 = \xi_3$, $x_5 = \xi_4$ and $x_6 = \xi_4$. The time coordinates t_i that enable the desired interference can be computed by similar travel time considerations as before, compare Eq. (19) to (24). The

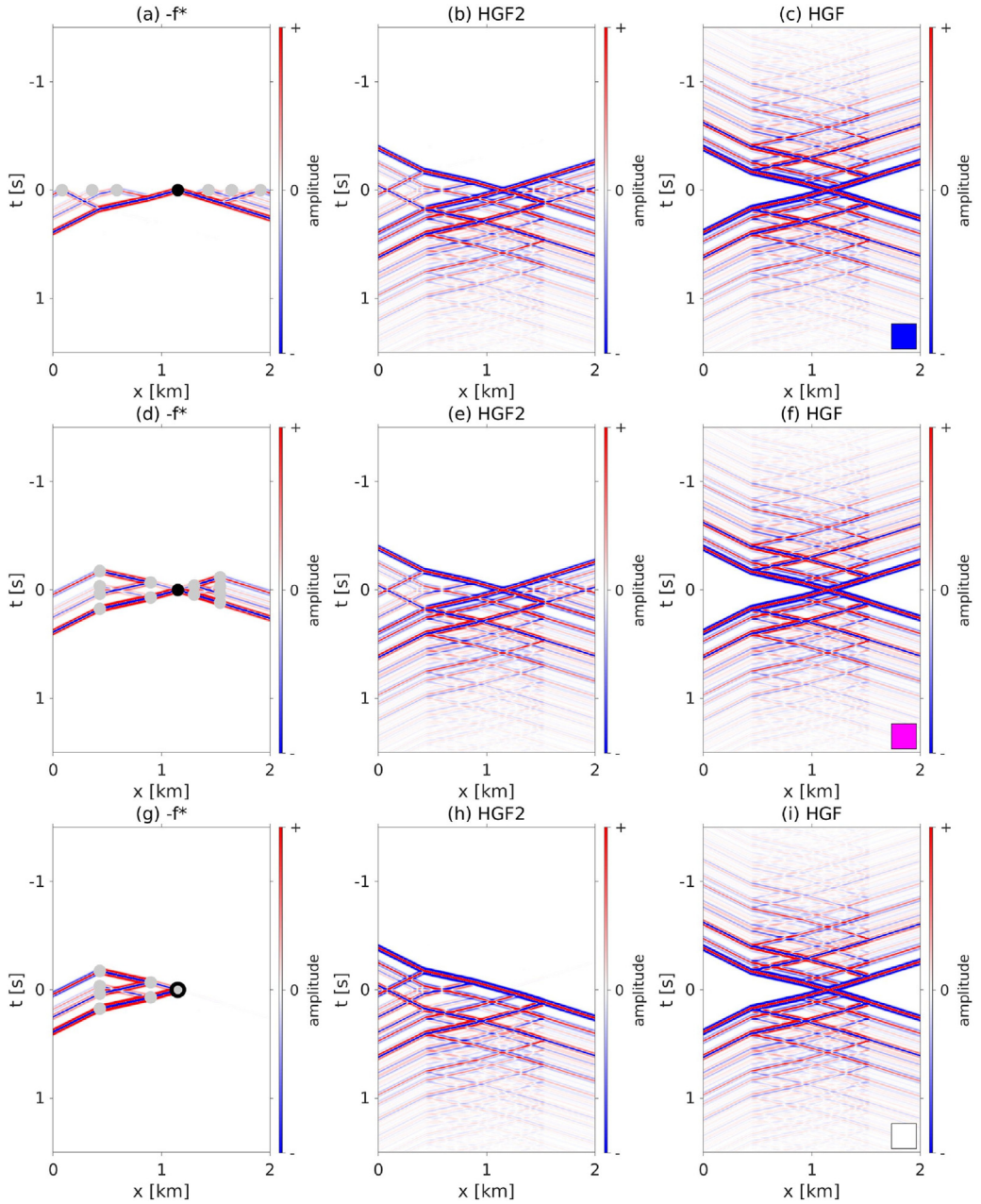

Fig. 6. Left column: negative, time-reversed time-compact focusing functions. Black dots mark the locations of the Green's function source at x_f, grey dots the locations of the source distributions $q(x, t; x_f)$. Central column: homogeneous Green's functions of the second kind. Right column: homogeneous Green's functions obtained from the homogeneous Green's functions of the second kind. (a), (b) and (c) are for double-sided $q(x, t; x_f)$ sources at zero time. (d), (e) and (f) are for double-sided $q(x, t; x_f)$ sources at the interfaces. (g), (h) and (i) are for single-sided $q(x, t; x_f)$ sources at the interfaces. (For interpretation of the references to colour in this figure legend, the reader is referred to the web version of this article.)

source $q_1(x, t; x_f)$ for instance has to emit energy when the negative, half-amplitude Green's function first arrives at the first interface. Since this is happening at a time different from zero, the two sources of $q_1(x, t; x_f)$ in Eq. (7) now appear distinctly separated in the sketch, one at $-t_1$ and one at t_1. Overall, we get the following time coordinates:

$$t_1 = t_3 + \frac{\xi_2 - \xi_1}{c_2} \tag{28}$$

$$t_2 = t_3 - \frac{\xi_2 - \xi_1}{c_2} \tag{29}$$

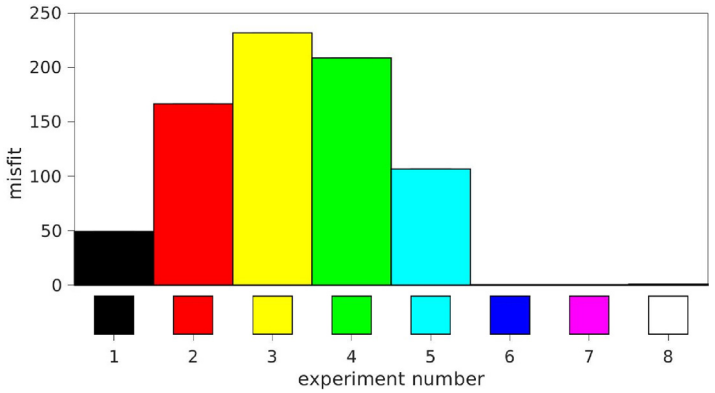

Fig. 7. Misfit between the actual homogeneous Green's function in Fig. 2(c) and the estimated homogeneous Green's functions obtained via the focusing functions. The colour encoding matches the rectangles in the bottom right corners of each of the estimated homogeneous Green's functions, i.e. experiment number 1 is for Fig. 3(c), 2 for Fig. 3(f), 3 for Fig. 3(i), 4 for Fig. 4(c), 5 for Fig. 4(f), 6 for Fig. 6(c), 7 for Fig. 6(f) and 8 for Fig. 6(i).

$$t_3 = \frac{x_f - \xi_2}{c_3} \tag{30}$$

$$t_4 = \frac{\xi_3 - x_f}{c_3} \tag{31}$$

$$t_5 = t_4 - \frac{\xi_4 - \xi_3}{c_4} \tag{32}$$

$$t_6 = t_4 + \frac{\xi_4 - \xi_3}{c_4} \quad , \tag{33}$$

where in contrast to the preceding source setup, all six sources always exist.

Similar to before, we can set up a linear system of equations for the weights. However, the amplitude considerations are more complex in this case because the dipole sources are located at interfaces, implying slightly modified radiation characteristics. In the preceding example, the dipoles were within the layers such that each source would emit a wave with same amplitude but reversed polarity into the two directions (leftwards and rightwards). For a dipole source at an interface, the leftwards propagating wave has an initial, unweighted amplitude (before any further transmission/reflection losses occur and without applying the individual weight w_i) proportional to

$$\mu_j = \frac{(\rho_j + \rho_{j+1})c(\xi_j)}{1 - \gamma_j} \quad , \tag{34}$$

where $c(\xi_j)$ is the velocity at the jth interface. While this velocity might be ill-defined, it is purely a constant scaling factor, making the assigned value irrelevant – we use $c(\xi_j) = (c_j + c_{j+1})/2$ for instance. Note that we only define four different amplitudes μ_j for the six sources since the initial, unweighted source amplitude only depends on the interface at which the source is located. Furthermore, we use $\gamma_j = -(1 + r_j)/(1 - r_j)$. The rightwards propagating wave has an initial, unweighted amplitude proportional to $\gamma_j \mu_j$. See Appendix A for details on the derivation of these amplitudes. Including the adjusted amplitudes we can follow the same recipe as before, i.e. for each area marked by a grey line in Fig. 8(a) we can sum up all the contributions from the different sources and set the result to zero. The linear system for the weights then reads

$$\begin{bmatrix} \gamma_1 & -r_1 r_2 \gamma_1 & -r_1 & -r_1(1-r_2) & 0 & -r_1(1-r_2)(1-r_3) \\ -r_1 r_2 \gamma_1 & \gamma_1 & -r_1 & 0 & 0 & 0 \\ 0 & (1+r_2)\gamma_1 & \gamma_2 & -r_2 & 0 & -r_2(1-r_3) \\ (1+r_2) r_3 \gamma_1 & 0 & r_3 \gamma_2 & 1 & 1-r_3 & 0 \\ 0 & 0 & 0 & r_4 \gamma_3 & 1 & -r_3 r_4 \\ (1+r_2)(1+r_3) r_4 \gamma_1 & 0 & (1+r_3) r_4 \gamma_2 & r_4 \gamma_3 & -r_3 r_4 & 1 \end{bmatrix} \begin{bmatrix} \mu_1 \\ \mu_1 \\ \mu_2 \\ \mu_3 \\ \mu_4 \\ \mu_4 \end{bmatrix}$$

$$\circ \begin{bmatrix} w_1 \\ w_2 \\ w_3 \\ w_4 \\ w_5 \\ w_6 \end{bmatrix} = \rho(x_f) c(x_f) \begin{bmatrix} -r_1(1-r_2)/2 \\ 0 \\ -r_2/2 \\ r_3/2 \\ 0 \\ (1+r_3) r_4/2 \end{bmatrix}, \tag{35}$$

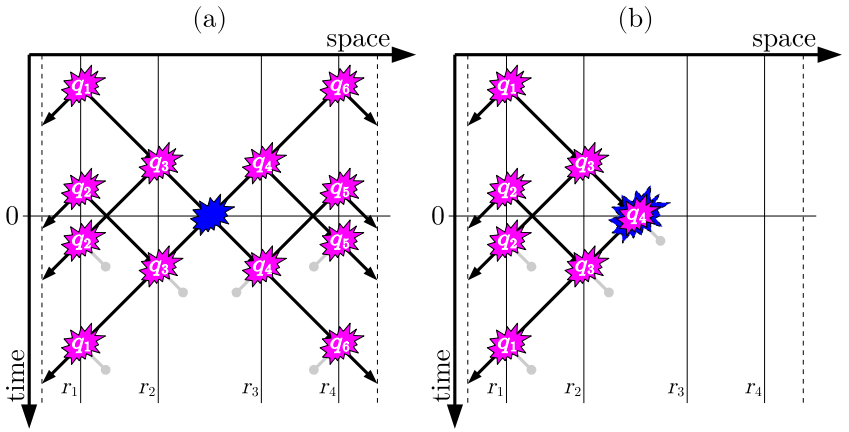

Fig. 8. Sketch of the time-reversed, time-compact focusing functions using (a) double-sided and (b) single-sided sources at the interfaces. The reflection coefficients r_1 mark the first interface, r_2 the second and so on. The blue explosions refer to the sources of the negative, half-amplitude Green's functions at x_f. The pink explosions denote the source distribution $q(x, t; x_f)$. Note that each q_i appears twice in this sketch, once at positive and once at negative time, and both together make up the actual source $q_i(x, t; x_f)$. The only exception is q_4 in (b), which is at zero time and thus denotes two overlapping sources. Furthermore, it overlaps with the source of the negative, half-amplitude Green's function — its blue explosion symbol is therefore increased in size to allow for a proper visualisation. The black arrows represent propagating events, the grey lines imply reflections which are suppressed in the time-compact focusing functions. (For interpretation of the references to colour in this figure legend, the reader is referred to the web version of this article.)

where we have nearly the same right hand side as before, but the matrix on the left hand side appears to be more complex due to the fact that the two sources in each $q_i(x, t; x_f)$ do not overlap in time any more. The inverse of this matrix exists for all physically reasonable cases, see Appendix B. After solving the above system for w_i we can model the negative, time-reversed focusing function using Eq. (6) where for the sources in Eq. (7) we have

$$q_i(x, t; x_f) = -w_i \rho(x) c(x_i) \big(\delta(t - t_i) + \delta(t + t_i)\big) \frac{\partial}{\partial x} \delta(x - x_i) \quad . \tag{36}$$

Again, note that the velocity $c(x_i)$ is only a constant scaling factor and not a function of x, whereas the density $\rho(x)$, which is different in the limits from above and below the interface, is under the action of the Dirac delta. The resulting negative, time-reversed focusing function for double-sided sources at the interfaces is shown in Fig. 6(d). Since there are sources at positive and negative times now, i.e. at $-t_i$ and t_i, this focusing function lives in a larger time window than the previous one. Note that the focusing functions on the boundaries of the volume, that is at $x = 0$ km and at $x = 2$ km, are exactly the same in both Figs. 6(a) and 6(d). In that sense the combined focusing functions $f\big(x, t; x_f, q(x, t; x_f)\big) - f\big(x, -t; x_f, q(x, t; x_f)\big)$, i.e. the wavefields in Eq. (10), are exactly the same. This illustrates the ambiguity of the source distribution $q(x, t; x_f)$. The source distribution of the new focusing function, see Fig. 6(d) for its negative, time-reversed version, however, is spatially more compact, i.e. there are no sources outside the scattering region of the volume. In other words, all sources are within the region between the first and the last interface, such that $q(x \notin V, t; x_f) = 0$ holds true for any volume that contains the scattering interfaces. When injecting the focusing function from the boundary, we get – as expected – the same homogeneous Green's function of the second kind as before, see Fig. 6(e). Fig. 6(f) gives the resulting homogeneous Green's function. As observed before, the accuracy of this homogeneous Green's function is higher than that of those retrieved via non-time-compact focusing functions, see Fig. 7.

Thus far, we illustrated how different sources $q(x, t; x_f)$ may deliver the same homogeneous Green's function of the second kind. For a focusing point in the third layer of a five layer medium, we have proven that one can always obtain a time-compact focusing function from double-side sources at the interfaces, such that $q(x, t; x_f) = 0$ everywhere beyond the scattering portion of the volume.

4.4.3. Single-sided sources at the interfaces

This final example is similar to the preceding one, but for the case of having sources only at locations $x_i \leq x_f$ — thus, we refer to this setup as single-sided (analogously, one could of course use sources only at locations $x_i \geq x_f$). Since we want to obtain the most time-compact focusing function, it follows that the focusing function should not penetrate any deeper than x_f. If there was energy propagating beyond this point it would induce scattering at the third and fourth interface and suppressing this scattering with sources at $x_i \leq x_f$ (if at all possible) would require a significantly larger time window for the focusing function. Hence, the most time-compact focusing functions for single-sided sources only propagate in a half-space, bounded by x_f. The source configuration is sketched in Fig. 8(b). While the time and space coordinates of $q_1(x, t; x_f)$, $q_2(x, t; x_f)$ and $q_3(x, t; x_f)$ remain unchanged compared to the preceding example sketched in

Fig. 8(a), $q_4(x, t; x_f)$ is now at $x_4 = x_f$ and $t_4 = 0$. Note that this is the only source which is not at an interface. Sources $q_5(x, t; x_f)$ and $q_6(x, t; x_f)$ become unnecessary in this setup, i.e. $n = 4$ in Eq. (7).

As depicted by the grey lines in Fig. 8(b) we have four equations that describe the annihilating wavefields of the four sources related to $q(x, t; x_f)$. The linear system reads

$$\begin{bmatrix} \gamma_1 & -r_1r_2\gamma_1 & -r_1 & -r_1(1-r_2) \\ -r_1r_2\gamma_1 & \gamma_1 & -r_1 & 0 \\ 0 & (1+r_2)\gamma_1 & \gamma_2 & -r_2 \\ (1+r_2)\gamma_1 & 0 & \gamma_2 & -1 \end{bmatrix} \begin{bmatrix} \mu_1 \\ \mu_1 \\ \mu_2 \\ 2\rho(x_f)c(x_f) \end{bmatrix} \circ \begin{bmatrix} w_1 \\ w_2 \\ w_3 \\ w_4 \end{bmatrix} = \rho(x_f)c(x_f) \begin{bmatrix} -r_1(1-r_2)/2 \\ 0 \\ -r_2/2 \\ 1/2 \end{bmatrix} \quad . \tag{37}$$

The determinant of this matrix is $(r_1+1)^2(r_2+1)$ which is different from zero for all $|r_1| < 1$ and $|r_2| < 1$, i.e. the inverse matrix exists for all physically reasonable scenarios. Using the time and space coordinates t_i and x_i as well as the weights we obtain from solving above system of equations for w_i, we can model the negative, time-reversed focusing function via Eq. (6), where for each of the $n = 4$ sources in Eq. (7) we use the relation given in Eq. (36).

The retrieved negative, time-reversed focusing function is shown in Fig. 6(g). It is similar to the previous result in Fig. 6(d), however, the wavefield now only propagates between $x = 0$ and $x = x_f$. Furthermore, the amplitudes are slightly different. The energy that is necessary to cancel the negative, half-amplitude Green's function in Eq. (8) comes solely from the left in this single-sided example — implying generally higher amplitudes for this focusing function. Note that this wavefield has quite an unusual appearance, being not only time-compact but also spatially bounded to the region to the left of x_f. This shows that we can inject energy into a medium such that it only propagates to one side. Measuring the wavefield at the other side will not show any arriving energy. But this is not due to attenuation, it is merely a consequence of choosing the correct sources for the medium under investigation, such that all rightwards travelling wavefields interfere destructively. As a consequence of the vanishing focusing function at the right boundary, we may choose to inject the focusing function from only the left boundary in Eq. (16). The homogeneous Green's function of the second kind is shown in Fig. 6(h). As before this wavefield is asymmetric in time. Furthermore, the spatial asymmetry is significantly more pronounced due to the single-sided source configuration, i.e. the entire top right corner (to the right of $x = x_f$ and above $t = 0$) is zero. The conventional homogeneous Green's function obtained from this result is given in Fig. 6(i). Note that this homogeneous Green's function is obtained from drastically reduced boundary data, i.e. we use a focusing function that is only different from zero on the left boundary and within a limited time window. Again, this homogeneous Green's function is a significantly better estimate than those obtained from non-time-compact focusing functions. However, due to an increased impact of numerical inaccuracies, the misfit is marginally higher than that of the previous two, double-sided experiments, see Fig. 7.

In summary, we presented and discussed different focusing functions in this section — going beyond those achievable by previous descriptions. In particular, we showed how to obtain time-compact focusing functions. While we did neither strictly prove that these time-compact focusing functions always exist for arbitrary 1D media nor describe how to obtain them in 2D and 3D, these examples clearly illustrate the concept of the source distribution $q(x, t; x_f)$ and how it can lead to perfect destructive interference and thereby time-compact wavefields. In that sense, our chosen benchmark examples demonstrate the applicability of the general equations in Section 3. Our main intention was to show how our new framework can be used to forward model focusing functions, i.e. how to obtain different types of focusing functions when given the physical properties of the medium. This is an important step in understanding focusing functions and might potentially lead to further progress, e.g., in inversion schemes based on focusing functions [54]. Furthermore this might be helpful in understanding the extent to which, e.g., single-sided focusing works in complex 2D and 3D media. The next section will discuss an approach to obtaining focusing functions without knowledge of the medium parameters.

5. Interferometry and Marchenko-like integrals

In the preceding sections we introduced and illustrated focusing functions and homogeneous Green's functions of the second kind. In this section we want to establish the connection of our work with the Marchenko integral by means of seismic interferometry [19,21,55,56]. In addition, we discuss the role of time-compact focusing functions.

Similar to time reversal modelling we can use reciprocity to obtain the interferometric relation

$$\frac{\partial}{\partial t} u(\boldsymbol{x_s}, t) = -\int_{\boldsymbol{x_r} \in \partial V} \int_{-\infty}^{\infty} \frac{2}{\rho(\boldsymbol{x_r})} \nabla g(\boldsymbol{x_r}, t-\tau; \boldsymbol{x_s}) u^{in}(\boldsymbol{x_r}, \tau) d\tau \cdot d\boldsymbol{S} \quad , \tag{38}$$

where ∂V is the closed boundary of a volume V that contains $\boldsymbol{x_s}$ and the wavefield $u(\boldsymbol{x}, t)$ has no sources in V [52,57]. Furthermore, the medium is supposed to be scattering-free outside the volume V such that the Green's function is a purely out-going wavefield. The wavefield $u^{in}(\boldsymbol{x}, t)$ is the part of the total field $u(\boldsymbol{x}, t)$ that is in-coming with respect to the bounded volume V. The gradient operator ∇ acts on the coordinate $\boldsymbol{x_r}$. Note that the equation involves a convolution of the Green's function and the in-coming wavefield $u^{in}(\boldsymbol{x}, t)$. This general relation allows for retrieving the full wavefield $u(\boldsymbol{x_s}, t)$ at $\boldsymbol{x_s}$ within the volume when knowing the in-coming field $u^{in}(\boldsymbol{x_r}, t)$ at $\boldsymbol{x_r}$ along the boundary as well as the Green's function $g(\boldsymbol{x_r}, t; \boldsymbol{x_s})$. Thus, it is necessary to have a source for the Green's function at $\boldsymbol{x_s}$ within the volume. For some applications this might be unrealistic because the interior of the volume V is inaccessible. In this case, we might have $\boldsymbol{x_s}$ to be just within the volume but very close to the boundary (in practice meaning that sources $\boldsymbol{x_s}$ and receivers

$\boldsymbol{x_r}$ of the Green's function are distributed along the surface of the volume of interest). This is the setup we will assume for the remaining part of this paper. Then, we can write Eq. (38) as

$$\frac{\partial}{\partial t}u^{out}(\boldsymbol{x_s},t) = -\int_{\boldsymbol{x_r}\in\partial V}\int_{-\infty}^{\infty}\frac{2}{\rho(\boldsymbol{x_r})}\nabla g(\boldsymbol{x_r},t-\tau;\boldsymbol{x_s})u^{in}(\boldsymbol{x_r},\tau)d\tau\cdot d\boldsymbol{S} \quad , \tag{39}$$

where using the spatial derivative of the Green's function only reconstructs the out-going part of the wavefield $u(\boldsymbol{x_s},t)$.

Let us take the homogeneous Green's function, Eq. (5), as a first example for a wavefield $u(\boldsymbol{x},t)$. This is indeed a source-free wavefield. Assuming that V contains $\boldsymbol{x_f}$, the in-coming part at ∂V is given by $g(\boldsymbol{x},-t;\boldsymbol{x_f})$ and the out-going part by $g(\boldsymbol{x},t;\boldsymbol{x_f})$. Thus, we obtain

$$\frac{\partial}{\partial t}g(\boldsymbol{x_s},t;\boldsymbol{x_f}) = -\int_{\boldsymbol{x_r}\in\partial V}\int_{-\infty}^{\infty}\frac{2}{\rho(\boldsymbol{x_r})}\nabla g(\boldsymbol{x_r},t+\tau;\boldsymbol{x_s})g(\boldsymbol{x_r},\tau;\boldsymbol{x_f})d\tau\cdot d\boldsymbol{S} \quad , \tag{40}$$

where we now have a correlation between the two Green's functions. Note that this representation excludes evanescent waves on the boundary, but contains the full wavefield inside the volume. This equation, however, is – for the same reasoning as before – not very useful since we are not necessarily able to have a source at $\boldsymbol{x_f}$ inside the volume.

For the homogeneous Green's function of the second kind on the other hand, we obtain the following equation:

$$\frac{\partial}{\partial t}\Big(g(\boldsymbol{x_s},t;\boldsymbol{x_f})+f\big(\boldsymbol{x_s},t;\boldsymbol{x_f},q(\boldsymbol{x},t)\big)\Big) = \int_{\boldsymbol{x_r}\in\partial V}\int_{-\infty}^{\infty}\frac{2}{\rho(\boldsymbol{x_r})}\nabla g(\boldsymbol{x_r},t+\tau;\boldsymbol{x_s})f\big(\boldsymbol{x_r},\tau;\boldsymbol{x_f},q(\boldsymbol{x},t)\big)d\tau\cdot d\boldsymbol{S} \quad , \tag{41}$$

where we assume that V contains $\boldsymbol{x_f}$ and $q(\boldsymbol{x}\notin V,t;\boldsymbol{x_f}) = 0$ such that $-f\big(\boldsymbol{x_r},-t;\boldsymbol{x_f},q(\boldsymbol{x},t)\big)$ is the only in-coming wavefield. This is the closed boundary representation that relates Green's and focusing functions for $\boldsymbol{x_s}$ near the boundary. As in the previous case, evanescent waves are only neglected on the boundary but accounted for inside the volume. Kiraz et al. [41] present another approach to obtain a similar closed boundary representation. Let us consider a special configuration where the volume is bounded by a horizontal plane ∂V_0 at $z=0$ and the surface of a half-sphere ∂V_1 below. Since we know that there are many different focusing functions, we are free to consider only the subset of focusing functions $-f\big(\boldsymbol{x_s},-t;\boldsymbol{x_f},\overline{q}(\boldsymbol{x},t;\boldsymbol{x_f})\big)$ that vanish at ∂V_1 – note that we use the source distribution $\overline{q}(\boldsymbol{x},t;\boldsymbol{x_f})$ to emphasise that this is a subset of focusing functions only. Furthermore, this source distribution generally depends on the focal location $\boldsymbol{x_f}$. We have already introduced an example of such a focusing function in Fig. 6(g). We do not actually prove the general existence of these focusing functions here — for complex media in two and three dimensions they might in fact not exist and investigating this remains a topic of ongoing research. Assuming that there are such focusing functions, Eq. (41) becomes

$$g(\boldsymbol{x_s},t;\boldsymbol{x_f})+f\big(\boldsymbol{x_s},t;\boldsymbol{x_f},\overline{q}(\boldsymbol{x},t;\boldsymbol{x_f})\big) = -\int_{\boldsymbol{x_r}\in\partial V_0}\int_{-\infty}^{\infty}r(\boldsymbol{x_r},t+\tau;\boldsymbol{x_s})f\big(\boldsymbol{x_r},\tau;\boldsymbol{x_f},\overline{q}(\boldsymbol{x},t;\boldsymbol{x_f})\big)d\tau\,d\boldsymbol{S} \quad , \tag{42}$$

with

$$\frac{\partial}{\partial t}r(\boldsymbol{x_r},t;\boldsymbol{x_s}) = \frac{2}{\rho(\boldsymbol{x_r})}\frac{\partial}{\partial z_r}g(\boldsymbol{x_r},t;\boldsymbol{x_s}) \quad . \tag{43}$$

This is the single-sided or open boundary representation. Note that this equation only holds for focusing functions that vanish on ∂V_1. It would not be sufficient to consider a focusing function that was purely out-going on ∂V_1: this would imply that the time-reversed focusing function was in-coming on ∂V_1 such that the integral over ∂V_1 would not vanish. The very same equation was derived in previous publications [18,58], however, involving several limitations regarding the Green's function. In particular, these derivations required up-/down-decomposition of the wavefields inside the volume as well as a truncated medium state, leading to a neglect of evanescent, refracted and diving waves. Our derivation does not involve any such assumptions, i.e. Eq. (42) contains the full wavefield Green's function inside the volume. Similar conclusions were recently presented by Wapenaar et al. [39], however, using a derivation built on a different definition of the focusing function. In particular, their focusing functions are source-free and focus on the surface ∂V_0 rather than inside the volume. Our scheme follows the concept introduced in [42], where focusing functions are related to a source term $q(\boldsymbol{x},t)$ and focus in space at $\boldsymbol{x_f}$ when injected into a source-free volume. This approach explains both closed and open boundary integral representations. Note that our Eq. (42) is slightly different from the conventional representation [18] because we define the negative, time-reversed auxiliary focal solution as the in-coming focusing function. Substituting $\phi\big(\boldsymbol{x_s},t;\boldsymbol{x_f},\overline{q}(\boldsymbol{x},t;\boldsymbol{x_f})\big) = -f\big(\boldsymbol{x_s},-t;\boldsymbol{x_f},\overline{q}(\boldsymbol{x},t;\boldsymbol{x_f})\big)$ yields the traditional form. This single-sided representation is interesting for several reasons, mainly: (i) it allows us to retrieve a Green's function by injecting a wavefield from only one side. This is rather unusual since interferometry (just like time reversal acoustics) for open boundaries is conventionally prone to artefacts, compare Eq. (40) where the time-reversed Green's function needs to be injected from the entire, closed boundary for accurate Green's function retrieval. (ii) Eq. (42) can (under circumstances) be solved for the focusing and Green's function when an estimate of the first arrival of the Green's function is available. The underlying assumption is that there is a focusing function $-f\big(\boldsymbol{x_s},-t;\boldsymbol{x_f},\hat{q}(\boldsymbol{x},t;\boldsymbol{x_f})\big)$ that is separated in time from the Green's function. We denote this additional constraint by the source $\hat{q}(\boldsymbol{x},t;\boldsymbol{x_f})$. This is where the previously introduced time-compact focusing functions come into play again, see Figs. 6(a), 6(d) and 6(g). Such a time-compact focusing function

only overlaps with the Green's function in the vicinity of the first arrival of the Green's function. Hence, we can define a window function $\theta(\boldsymbol{x_s}, t; \boldsymbol{x_f})$ that removes all arrivals before $-t_{first}(\boldsymbol{x_s}; \boldsymbol{x_f})$ and after $t_{first}(\boldsymbol{x_s}; \boldsymbol{x_f})$, where $t_{first}(\boldsymbol{x_s}; \boldsymbol{x_f})$ is the time of the first arrival of the wavefield for a source at $\boldsymbol{x_f}$ and a receiver at $\boldsymbol{x_s}$ [18,59–61]. In other words, we have $\theta(\boldsymbol{x_s}, t; \boldsymbol{x_f}) = 0$ for all $|t| > t_{first}(\boldsymbol{x_s}; \boldsymbol{x_f})$ and $\theta(\boldsymbol{x_s}, t; \boldsymbol{x_f}) = 1$ otherwise. Applying the window operator to Eq. (42) we get:

$$g_{first}(\boldsymbol{x_s}, t; \boldsymbol{x_f}) + f\left(\boldsymbol{x_s}, t; \boldsymbol{x_f}, \hat{q}(\boldsymbol{x}, t; \boldsymbol{x_f})\right) = -\theta(\boldsymbol{x_s}, t; \boldsymbol{x_f}) \int_{\boldsymbol{x_r} \in \partial V_0} \int_{-\infty}^{\infty} r(\boldsymbol{x_r}, t + \tau; \boldsymbol{x_s}) f\left(\boldsymbol{x_r}, \tau; \boldsymbol{x_f}, \hat{q}(\boldsymbol{x}, t; \boldsymbol{x_f})\right) d\tau \, d\boldsymbol{S} \quad . \tag{44}$$

This expression is a Marchenko-like integral [11–15,62]. Assuming that the first arrival of the Green's function $g_{first}(\boldsymbol{x_s}, t; \boldsymbol{x_f})$ is known (e.g. from modelling in a smooth estimate of the medium), the equation contains only one unknown quantity, i.e. the focusing function. Thus, we can solve for the focusing function and, subsequently, via Eq. (42) for the Green's function. Since the focus of this paper is on the derivation of the representations and not on their solutions, we refer the interested reader to other papers for the traditional approach [18,60] or for a solution without up-/down-decomposed fields [38]. This equation forms the basis for many applications in geophysics, e.g. Green's function retrieval, multiple elimination and Marchenko imaging.

In this section we connected the insights from the previous sections with the concept of single-sided Green's function retrieval, i.e. we derived a Marchenko-like equation without up-/down-decomposition of the wavefields based on a partial differential equation framework for focusing functions. Note that we did not imply that solutions $f\left(\boldsymbol{x_s}, t; \boldsymbol{x_f}, \hat{q}(\boldsymbol{x}, t; \boldsymbol{x_f})\right)$ always exist for arbitrary media and conditions. However, we may say that if we find a focusing function using such an approach it obviously exists and obeys our constraints, i.e. it vanishes at ∂V_1 and is separated from the Green's function in time. So far, our experience with numerical examples confirms solutions do often exist and can be retrieved from boundary data, but to what extent that is the case in general is the subject of ongoing research. Our derivation does not include any approximations regarding the Green's function, i.e. if the focusing function exists under our constraints the reconstructed Green's function will contain the full-spectrum.

6. Discussion

In this paper, we discuss and illustrate a new, generalised framework for wavefield focusing. Building on the concept introduced in [38] we add explanations to the definition of the focusing function as well as its relation to the Green's function. The underlying partial differential equation allows us to obtain the homogeneous Green's function of the second kind, a source-free, potentially asymmetric wavefield that contains the causal Green's function. This potential asymmetry stems from the fact that the homogeneous Green's function of the second kind comprises one in-coming field, i.e. the focusing function, and two out-going fields, i.e. the negative, time-reversed focusing function and the Green's function. When adding the homogeneous Green's function of the second kind and its time-reversed version, one always obtains the conventional homogeneous Green's function. This unifying property of focusing functions, or more precisely of their respective homogeneous Green's functions of the second kind, also implies a focus in space of the homogeneous Green's functions of the second kind at $\boldsymbol{x_f}$ and zero time. It is due to this focus that we call the underlying fields focusing functions. Focusing functions have already been studied in the context of Marchenko-based schemes in geophysics [18,60], however, our new definition generalises the concept of focusing and establishes a source term that enables modelling of focusing functions.

The numerical examples illustrate the concept of focusing and show how focusing functions can be built to destructively interfere with the local Green's function. Ultimately, we can construct focusing functions which are compact in time and, if desired, vanish on particular parts of the boundary. Using such time-compact focusing functions rather than Green's functions for time reversal modelling actually enables a superior accuracy of the retrieved homogeneous Green's functions. We find that the source distribution $q(\boldsymbol{x}, t)$ that governs the focusing function might be ambiguous, i.e. different sources deliver the same combined focusing functions $f\left(\boldsymbol{x_s}, t; \boldsymbol{x_f}, q(\boldsymbol{x}, t)\right) - f\left(\boldsymbol{x_s}, -t; \boldsymbol{x_f}, q(\boldsymbol{x}, t)\right)$. Although the numerical examples are in 1D, we think that similar approaches exist for 2D and 3D. These approaches will have to be more elaborate though, including, e.g. geometrical spreading and angle-dependent reflection coefficients. The results presented in this paper illustrate how we can use the full (two-way) wave equation to model time-compact focusing wavefields. Using a different approach, Elison et al. [63] recently presented modelled focusing functions in 2D. The way that we constructed the time-compact focusing fields is very example-specific and a generalisation to arbitrary media (as well as to 2D and 3D) is a topic for future research. The main goal of the numerical examples in this paper is simply the illustration of focusing functions in the light of our new definition.

The implications of our approach go beyond the ability to model focusing functions and increase the accuracy of time reversal acoustics. We also derived representations for Green's and focusing functions without up-/down-decomposed wavefields or a truncated medium assumption, suggesting that our derivation includes the full wavefield Green's function, involving diving, refracted and evanescent waves. Since we present a unified approach to wavefield focusing, we can derive such integrals for both closed and open boundary systems as both follow in a straightforward fashion from our underlying theory. The closed boundary representation is entirely general, i.e. valid for any focusing function. The open boundary representation on the other hand requires that the associated focusing function vanishes on the remaining boundary, i.e. this integral is only valid for a subset of focusing functions. In fact, it might even be that the open boundary representation is only valid for one unique focusing function (or none at all in complex media) since Eq. (42) can often

be directly inverted for $-f\left(\boldsymbol{x}_{\boldsymbol{s}}, -t; \boldsymbol{x}_{\boldsymbol{f}}, \overline{q}(\boldsymbol{x}, t; \boldsymbol{x}_{\boldsymbol{f}})\right)$ when the Green's function is given [35]. If we want to solve the integral for the focusing and Green's functions based on an estimate of the first arrival Green's function we additionally need to assume that focusing and Green's functions can be separated in time. Using this separability assumption we obtain a Marchenko-like equation. It remains to be investigated, when exactly Eqs. (42) and (44) break, i.e. when and to what extent single-sided focusing in 2D and 3D becomes implausible. The separability assumption used in Eq. (44) to solve the representation for focusing and Green's functions is known to fail for complex velocity and density models in 2D and 3D due to the related scattering patterns, including, e.g., diffractions [35,64,65]. Hence, even if there is a unique, single-sided focusing function $-f\left(\boldsymbol{x}_{\boldsymbol{s}}, -t; \boldsymbol{x}_{\boldsymbol{f}}, \overline{q}(\boldsymbol{x}, t; \boldsymbol{x}_{\boldsymbol{f}})\right)$ for Eq. (42) it might not necessarily obey the time-separability constraint [35].

We suspect that our new partial differential equation approach might help to investigate these questions further. The underlying partial differential equations might also prove useful when it comes to combining Marchenko-like approaches with full waveform inversion [54,66–69]. In 1D it is known how to extract the scattering potential from the focusing functions directly [46,70–72]. For higher dimensions we might gain further understanding of the relation between the focusing function and the scattering potential by studying our scheme more explicitly in 2D and 3D. Last but not least, our derivation shows that the representations, e.g., Eq. (42) include the full wave Green's function. This might allow for more advanced data applications and experiments in the future, including evanescent, refracted and diving waves.

7. Conclusions

We present a partial differential equation framework for generalised wavefield focusing. In particular we define focusing functions that govern the homogeneous Green's function of the second kind. These homogeneous Green's functions of the second kind can be quite asymmetric both in time and space, but they always have a focus in space at $\boldsymbol{x}_{\boldsymbol{f}}$ and zero time. Furthermore, they deliver the conventional homogeneous Green's function when adding their time-reversed version. While our definition generalises the idea of focusing functions that were previously introduced in the context of Marchenko-like schemes, it also represents an entirely new way to describe these functions, paving the way for new insights and improved understanding. We discuss and illustrate different families of focusing functions with numerical examples, where our partial differential equation framework allows us to go beyond focusing functions described in previous approaches. In particular, we demonstrate how our equations allow for constructing time-compact focusing functions for closed and open boundary systems. Last but not least, we use reciprocity to obtain Marchenko-like integrals that relate focusing and Green's functions based on the homogeneous Green's function of the second kind. Owing to the unifying character of our wavefield focusing approach, we obtain these Marchenko-like integral representations for both closed and open boundaries. This derivation does not require up-/down-decomposed wavefields inside the medium and thus circumvents the limitations of most previous approaches.

CRediT authorship contribution statement

Leon Diekmann: Conceptualization, Methodology, Software, Writing – original draft, Visualization. **Ivan Vasconcelos:** Conceptualization, Resources, Writing – review & editing, Supervision, Funding acquisition. **Kees Wapenaar:** Writing – review & editing, Supervision. **Evert Slob:** Writing – review & editing, Supervision. **Roel Snieder:** Writing – review & editing, Supervision.

Declaration of competing interest

The authors declare the following financial interests/personal relationships which may be considered as potential competing interests: Leon Diekmann reports financial support was provided by Utrecht Consortium for Subsurface Imaging (UCSI). The following companies sponsor the UCSI: Equinor ASA, Total E&P, Petrobras, Aramco Overseas.

Data availability

No data was used for the research described in the article.

Acknowledgements

The authors are thankful to Dirk-Jan van Manen, David Vargas, Andreas Tataris, Haorui Peng and Tristan van Leeuwen for discussions. Leon Diekmann is financially supported by the Utrecht Consortium for Subsurface Imaging (UCSI). Kees Wapenaar acknowledges funding from the European Research Council (ERC) under the European Union's Horizon 2020 research and innovation programme (grant agreement 742703). The authors are grateful to Giovanni Angelo Meles and an anonymous reviewer for their constructive feedback that helped to improve the paper.

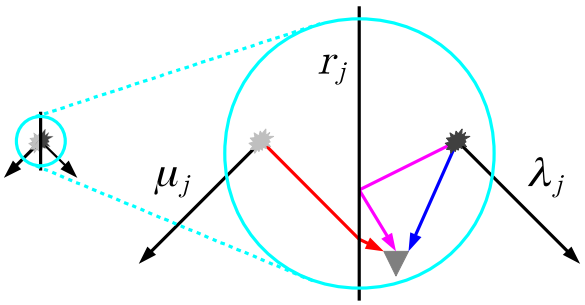

Fig. 9. Sketch of a dipole source at an interface. Left: apparent source. Right: actual source used for modelling, consisting of two monopole sources. The reflectivity is denoted by r_j, μ_j and λ_j are proportional to the amplitudes of the apparent dipole source.

Appendix A. Dipole source amplitudes at interfaces

In order to compute the amplitudes for a dipole source at an interface we have to exploit two relations: (i) the direct wavefield at the interface itself should have zero amplitude and (ii) the total emitted energy should be proportional to the physical properties of the medium around the interface. As stated in the text, we mimic the dipole by two monopoles with opposite polarity. Thus, one monopole is above the interface and the other below, see also Fig. 9. Considering the point denoted by the triangle in this sketch, which is supposed to be infinitesimally far away from the interface, the first relation (i) means that the three direct field contributions indicated by the blue, magenta and red arrows cancel each other. This gives

$$\mu_j(1+r_j)+\lambda_j(1-r_j)=0 \quad , \tag{45}$$

where μ_j and λ_j are proportional to the amplitudes of the dipole source as sketched in Fig. 9, μ_j is positive and λ_j is negative. The second relation (ii) can be described by

$$|\mu_j|+|\lambda_j|=\mu_j-\lambda_j=(\rho_j+\rho_{j+1})c(\xi_j) \quad , \tag{46}$$

i.e. the amplitudes are proportional to the densities of the layers above and below the interface, scaled by an arbitrary velocity. From Eq. (45) we obtain $\lambda_j/\mu_j=-(1+r_j)/(1-r_j)$ which equals the previously defined γ_j. Thus, the rightwards propagating wave has an initial, unweighted amplitude proportional to $\lambda_j=\gamma_j\mu_j$. Dividing Eq. (46) by μ_j and using $\lambda_j/\mu_j=\gamma_j$ we obtain Eq. (34).

Appendix B. Existence of inverse matrix in Eq. (35)

The determinant of the matrix in Eq. (35) is

$$-(r_1+1)^2(r_4+1)(r_2+1)(r_1r_2+r_1r_3+r_1r_4+r_2r_3+r_2r_4+r_3r_4+r_1r_2r_3r_4+1)(r_1-1)^{-1}(r_2-1)^{-1} \quad , \tag{47}$$

where for all terms except for the fourth one it is straightforward to see that they are always different from zero for $|r_j|<1$ with $j=1,2,3,4$. The fourth term is zero for

$$r_1=-\frac{r_2r_3+r_2r_4+r_3r_4+1}{r_2+r_3+r_4+r_2r_3r_4} \quad , \tag{48}$$

or regarding the absolute value

$$|r_1|=\left|\frac{r_2r_3+r_2r_4+r_3r_4+1}{r_2+r_3+r_4+r_2r_3r_4}\right|=\left|\frac{\mathfrak{p}+r_4}{1+\mathfrak{p}r_4}\right|\geq 1 \quad , \tag{49}$$

with $\mathfrak{p}=(1+r_2r_3)/(r_2+r_3)$. By showing that the right-most inequality above holds true, we prove that the determinant can never be zero for the ranges of physically reasonable reflection coefficients that we consider. The inequality can be rewritten according to

$$(\mathfrak{p}+r_4)^2\geq(1+\mathfrak{p}r_4)^2\Leftrightarrow\mathfrak{p}^2-1\geq r_4^2(\mathfrak{p}^2-1)\Leftrightarrow 1\geq|r_4| \quad , \tag{50}$$

where the last inequality follows if $|\mathfrak{p}|>1$ and then is true because we have $|r_4|<1$. Thus, we have to show that

$$|\mathfrak{p}|>1\Leftrightarrow(1+r_2r_3)^2>(r_2+r_3)^2\Leftrightarrow r_2^2(r_3^2-1)>r_3^2-1\Leftrightarrow|r_2|<1 \quad , \tag{51}$$

where we use $r_3^2-1<0$ for $|r_3|<1$ to obtain the last inequality. This last inequality is true such that the determinant is always different from zero for $|r_j|<1$ with $j=1,2,3,4$.

References

[1] K. Chadan, P.C. Sabatier, Inverse Problems in Quantum Scattering Theory, Springer Science & Business Media, 2012.
[2] D.L. Colton, R. Kress, Inverse Acoustic and Electromagnetic Scattering Theory, Vol. 93, Springer.
[3] P. Deift, E. Trubowitz, Inverse scattering on the line, Comm. Pure Appl. Math. 32 (2) (1979) 121–251.
[4] R. Jost, Inverse Scattering Problems in Optics, Vol. 20, Springer Science & Business Media, 2012.
[5] A.B. Weglein, F.A. Gasparotto, P.M. Carvalho, R.H. Stolt, An inverse-scattering series method for attenuating multiples in seismic reflection data, Geophysics 62 (6) (1997) 1975–1989.
[6] M. Zuberi, T. Alkhalifah, Generalized internal multiple imaging (GIMI) using Feynman-like diagrams, Geophys. J. Int. 197 (3) (2014) 1582–1592.
[7] T. Alkhalifah, Q. Guo, Subsurface wavefields based on the generalized internal multiple imaging, Geophys. J. Int. 219 (2) (2019) 1212–1224.
[8] J.D. Shea, P. Kosmas, S.C. Hagness, B.D. Van Veen, Three-dimensional microwave imaging of realistic numerical breast phantoms via a multiple-frequency inverse scattering technique, Med. Phys. 37 (8) (2010) 4210–4226.
[9] J.H. Rose, Elastic wave inverse scattering in nondestructive evaluation, in: Scattering and Attenuation of Seismic Waves, Part II, Springer, 1989, pp. 715–739.
[10] V.A. Marchenko, On reconstruction of the potential energy from phases of the scattered waves, in: Doklady Akademii Nauk SSSR, vol. 104, (no. 5) 1955, pp. 695–698.
[11] R. Burridge, The Gelfand-Levitan, the Marchenko, and the Gopinath-Sondhi integral equations of inverse scattering theory, regarded in the context of inverse impulse-response problems, Wave Motion 2 (4) (1980) 305–323.
[12] R.G. Newton, Inverse scattering. I. One dimension, J. Math. Phys. 21 (3) (1980) 493–505.
[13] J.H. Rose, 'Single-sided' focusing of the time-dependent Schrödinger equation, Phys. Rev. A 65 (1) (2001) 012707.
[14] J.H. Rose, 'Single-sided' autofocusing of sound in layered materials, Inverse Problems 18 (6) (2002) 1923.
[15] F. Broggini, R. Snieder, K. Wapenaar, Focusing the wavefield inside an unknown 1D medium: Beyond seismic interferometry, Geophysics 77 (5) (2012) A25–A28.
[16] F. Broggini, R. Snieder, Connection of scattering principles: A visual and mathematical tour, Eur. J. Phys. 33 (3) (2012) 593.
[17] K. Wapenaar, J. Thorbecke, J. van der Neut, F. Broggini, E. Slob, R. Snieder, Green's function retrieval from reflection data, in absence of a receiver at the virtual source position, J. Acoust. Soc. Am. 135 (5) (2014) 2847–2861.
[18] K. Wapenaar, J. Thorbecke, J. Van Der Neut, F. Broggini, E. Slob, R. Snieder, Marchenko imaging, Geophysics 79 (3) (2014) WA39–WA57.
[19] G. Schuster, Seismic Interferometry, Cambridge University Press, 2009.
[20] A. Bakulin, R. Calvert, The virtual source method: Theory and case study, Geophysics 71 (4) (2006) SI139–SI150.
[21] A. Curtis, P. Gerstoft, H. Sato, R. Snieder, K. Wapenaar, Seismic interferometry – turning noise into signal, Leading Edge 25 (9) (2006) 1082–1092.
[22] K. Löer, G.A. Meles, A. Curtis, I. Vasconcelos, Diffracted and pseudo-physical waves from spatially limited arrays using source–receiver interferometry (SRI), Geophys. J. Int. 196 (2) (2014) 1043–1059.
[23] K. Wapenaar, J. Thorbecke, Virtual sources and their responses, Part I: Time-reversal acoustics and seismic interferometry, Geophys. Prospect. 65 (6) (2017) 1411–1429.
[24] K. Wapenaar, J. Thorbecke, J. van der Neut, E. Slob, R. Snieder, Virtual sources and their responses, Part II: Data-driven single-sided focusing, Geophys. Prospect. 65 (6) (2017) 1430–1451.
[25] M. Ravasi, I. Vasconcelos, A. Kritski, A. Curtis, C.A.d.C. Filho, G.A. Meles, Target-oriented marchenko imaging of a North Sea field, Geophys. Suppl. Mon. Not. R. Astron. Soc. 205 (1) (2016) 99–104.
[26] L. Zhang, E. Slob, Free-surface and internal multiple elimination in one step without adaptive subtraction, Geophysics 84 (1) (2019) A7–A11.
[27] M. Staring, K. Wapenaar, Three-dimensional Marchenko internal multiple attenuation on narrow azimuth streamer data of the Santos Basin, Brazil, Geophys. Prospect. 68 (6) (2020) 1864–1877.
[28] J. Brackenhoff, J. Thorbecke, K. Wapenaar, Monitoring of induced distributed double-couple sources using Marchenko-based virtual receivers, Solid Earth 10 (4) (2019) 1301–1319.
[29] J. van IJsseldijk, K. Wapenaar, Discerning small time-lapse traveltime changes by isolating the seismic response of a reservoir using the Marchenko method, in: First International Meeting for Applied Geoscience & Energy, Society of Exploration Geophysicists, 2021, pp. 3449–3453.
[30] C.A. da Costa Filho, M. Ravasi, A. Curtis, G.A. Meles, Elastodynamic Green's function retrieval through single-sided Marchenko inverse scattering, Phys. Rev. E 90 (6) (2014) 063201.
[31] C. Reinicke, K. Wapenaar, Elastodynamic single-sided homogeneous Green's function representation: Theory and numerical examples, Wave Motion 89 (2019) 245–264.
[32] C. Reinicke, M. Dukalski, K. Wapenaar, Comparison of monotonicity challenges encountered by the inverse scattering series and the Marchenko demultiple method for elastic waves, Geophysics 85 (5) (2020) Q11–Q26.
[33] J. Van der Neut, J. Brackenhoff, G.A. Meles, E. Slob, K. Wapenaar, Marchenko Green's function retrieval in layered elastic media from two-sided reflection and transmission data, Appl. Sci. 12 (15) (2022) 7824.
[34] I. Vasconcelos, Y. Sripanich, Scattering-based Marchenko for subsurface focusing and redatuming in highly complex media, in: 81st EAGE Conference and Exhibition 2019, Vol. 2019, no. 1, European Association of Geoscientists & Engineers, 2019, pp. 1–5.
[35] D. Vargas, I. Vasconcelos, Y. Sripanich, M. Ravasi, Scattering-based focusing for imaging in highly complex media from band-limited, multi-component data, Geophysics 86 (5) (2021) 1–64.
[36] K. Wapenaar, The marchenko method for evanescent waves, Geophys. J. Int. 223 (2) (2020) 1412–1417.
[37] M.S. Kiraz, R. Snieder, K. Wapenaar, Marchenko without up/down decomposition on the Marmousi model and retrieval of the refracted waves: Are they caused by the Marchenko algorithm? in: First International Meeting for Applied Geoscience & Energy, Society of Exploration Geophysicists, 2021, pp. 3280–3284.
[38] L. Diekmann, I. Vasconcelos, Focusing and Green's function retrieval in three-dimensional inverse scattering revisited: A single-sided Marchenko integral for the full wave field, Phys. Rev. Res. 3 (1) (2021) 013206.
[39] K. Wapenaar, R. Snieder, S. de Ridder, E. Slob, Green's function representations for Marchenko imaging without up/down decomposition, Geophys. J. Int. 227 (1) (2021) 184–203.
[40] G.A. Meles, J. Van Der Neut, K.W. Van Dongen, K. Wapenaar, Wavefield focusing with reduced cranial invasiveness, in: 2019 IEEE International Ultrasonics Symposium, IUS, IEEE, 2019, pp. 1851–1854.
[41] M.S. Kiraz, R. Snieder, K. Wapenaar, Focusing waves in an unknown medium without wavefield decomposition, JASA Express Lett. 1 (5) (2021) 055602.
[42] L. Diekmann, I. Vasconcelos, Full-wavefield marchenko using a generalized framework for focusing functions, in: First International Meeting for Applied Geoscience & Energy, Society of Exploration Geophysicists, 2021, pp. 3311–3315.
[43] M.L. Oristaglio, An inverse scattering formula that uses all the data, Inverse Problems 5 (6) (1989) 1097.
[44] J.H. Rose, Time reversal, focusing and exact inverse scattering, in: Imaging of Complex Media with Acoustic and Seismic Waves, Springer, 2002, pp. 97–106.
[45] M. Fink, Time-reversal acoustics, J. Phys.: Conf. Ser. 118 (1) (2008) 012001.

[46] G.L. Lamb Jr., Elements of Soliton Theory, New York, 1980, p. 29.
[47] R. Snieder, K. Wapenaar, U. Wegler, Unified Green's function retrieval by cross-correlation; Connection with energy principles, Phys. Rev. E 75 (3) (2007) 036103.
[48] K. Wapenaar, H. Douma, A unified optical theorem for scalar and vectorial wave fields, J. Acoust. Soc. Am. 131 (5) (2012) 3611–3626.
[49] A.T. de Hoop, Handbook of Radiation and Scattering of Waves, Academic Press, 1995.
[50] N. Ricker, Wavelet contraction, wavelet expansion, and the control of seismic resolution, Geophysics 18 (4) (1953) 769–792.
[51] M. Fink, Time reversal of ultrasonic fields. I. Basic principles, IEEE Trans. Ultrason. Ferroelectr. Freq. Control 39 (5) (1992) 555–566.
[52] J.T. Fokkema, P.M. van den Berg, Seismic Applications of Acoustic Reciprocity, Elsevier, 2013.
[53] R. Snieder, K. Van Wijk, A Guided Tour of Mathematical Methods for the Physical Sciences, Cambridge University Press, 2015.
[54] L. Diekmann, I. Vasconcelos, D. Cummings, A. Curtis, Towards exact linearized full-waveform inversion via Marchenko redatuming, in: First International Meeting for Applied Geoscience & Energy, Society of Exploration Geophysicists, 2021, pp. 3380–3384.
[55] K. Wapenaar, D. Draganov, R. Snieder, X. Campman, A. Verdel, Tutorial on seismic interferometry: Part 1 – Basic principles and applications, Geophysics 75 (5) (2010) 75A195–75A209.
[56] K. Wapenaar, E. Slob, R. Snieder, A. Curtis, Tutorial on seismic interferometry: Part 2 – underlying theory and new advances, Geophysics 75 (5) (2010) 75A211–75A227.
[57] K. Wapenaar, General representations for wavefield modeling and inversion in geophysics, Geophysics 72 (5) (2007) SM5–SM17.
[58] K. Wapenaar, F. Broggini, E. Slob, R. Snieder, Three-dimensional single-sided Marchenko inverse scattering, data-driven focusing, Green's function retrieval, and their mutual relations, Phys. Rev. Lett. 110 (8) (2013) 084301.
[59] K. Wapenaar, F. Broggini, R. Snieder, Creating a virtual source inside a medium from reflection data: Heuristic derivation and stationary-phase analysis, Geophys. J. Int. 190 (2) (2012) 1020–1024.
[60] J. van der Neut, I. Vasconcelos, K. Wapenaar, On Green's function retrieval by iterative substitution of the coupled Marchenko equations, Geophys. J. Int. 203 (2) (2015) 792–813.
[61] L. Zhang, E. Slob, J. van der Neut, K. Wapenaar, Artifact-free reverse time migration, Geophysics 83 (5) (2018) A65–A68.
[62] R.-S. Wu, J. You, Time-boundary reflection/transmission and the dual fundamental solution in inverse scattering, in: First International Meeting for Applied Geoscience & Energy, Society of Exploration Geophysicists, 2021, pp. 3296–3300.
[63] P. Elison, M. Dukalski, D. Van Manen, Quality control of under-constrained Marchenko equation solvers in complex media using reference focusing functions, in: 82nd EAGE Annual Conference & Exhibition, Vol. 2021, no. 1, European Association of Geoscientists & Engineers, 2021, pp. 1–5.
[64] B. Schwarz, An introduction to seismic diffraction, in: Advances in Geophysics, vol. 60, Elsevier, 2019, pp. 1–64.
[65] J. Van der Neut, J. Brackenhoff, G. Meles, L. Zhang, E. Slob, K. Wapenaar, On the benefits of auxiliary transmission data for Marchenko-based Green's function retrieval, in: 82nd EAGE Annual Conference & Exhibition, Vol. 2021, no. 1, European Association of Geoscientists & Engineers, 2021, pp. 1–5.
[66] J. Virieux, S. Operto, An overview of full-waveform inversion in exploration geophysics, Geophysics 74 (6) (2009) WCC1–WCC26.
[67] T. Cui, J. Rickett, I. Vasconcelos, B. Veitch, Target-oriented full-waveform inversion using Marchenko redatumed wavefields, Geophys. J. Int. 223 (2) (2020) 792–810.
[68] L. Diekmann, I. Vasconcelos, Imaging with the exact linearised Lippmann-Schwinger integral by means of redatumed in-volume wavefields, in: SEG International Exposition and Annual Meeting, OnePetro, 2020.
[69] S.A. Shoja, G.A. Meles, K. Wapenaar, A proposal for Marchenko-based target-oriented full waveform inversion, in: 82nd EAGE Annual Conference & Exhibition, Vol. 2020, no. 1, European Association of Geoscientists & Engineers, 2020, pp. 1–5.
[70] Z. Agranovich, V.A. Marchenko, The Inverse Problem of Scattering Theory, Courier Dover Publications, 2020.
[71] J.A. Ware, K. Aki, Continuous and discrete inverse-scattering problems in a stratified elastic medium. I. Plane waves at normal incidence, J. Acoust. Soc. Am. 45 (4) (1969) 911–921.
[72] E. Slob, K. Wapenaar, S. Treitel, Tutorial: Unified 1D inversion of the acoustic reflection response, Geophys. Prospect. 68 (5) (2020) 1425–1442.